J Adv Ceram

Research Article

High entropy silicate ceramic aerogels with excellent thermal stability up to 1600 °C and their fiber-reinforced composites for high temperature insulation

Sisi Shang[1,2], Zhun Fan[1], Jing Fang[1], Man Yuan[1,2], Zihao Song[1,2], Wei Liu[1,2], Jian Yang[1,2,✉], Sheng Cui[1,2,✉]

Cite this article: Shang S, Fan Z, Fang J, et al. *J Adv Ceram* 2026, **15**(1): 9221217. https://doi.org/10.26599/JAC.2025.9221217

ABSTRACT: Ceramic aerogels have promising applications in extreme environments, such as aerospace, but are severely limited by the sintering-prone nature of nanounits at high temperatures. However, they typically exhibit inadequate dimensional stability when exposed to high-temperature atmospheres, which can result in the deterioration of their macroscopic characteristics, eventually restricting their applications in extreme environments. Here, a $(YYbErDyGd)_2SiO_5$ ceramic aerogel (ESA) was prepared at 1050 °C by introducing high entropy into a ceramic aerogel, thereby enhancing its high-temperature thermal stability via the high-entropy effect. ESA was exposed to a temperature of 1600 °C for 2 h without undergoing sintering. In addition, different fiber-reinforced ceramic aerogel composites are also explored, with a thermal conductivity of only 0.032 W/(m·K) at room temperature and 0.108 W/(m·K) at high temperature of 1000 °C. These composites demonstrate no visible damage or deformation under extreme conditions across a substantial temperature range (−196 to 1300 °C), a property that is paramount for applications in extreme environments. At 1100–1300 °C, after 2 h of calcination, the composites exhibit a shrinkage rate of only 0.25%. After 600 s of butane torch ablation at 1300 °C, the back temperature is only 110 °C. Moreover, under 60% compression deformation, its maximum compression strength is 0.386 MPa. Even after 20 high-temperature thermal cycles (1300 °C for 2 h), the sample maintains a low thermal conductivity of 0.043 W/(m·K) and a compressive strength of 0.259 MPa. This work provides a new perspective for exploring the limits of the strength and thermal properties of ceramic composites in the field of high-temperature insulation, particularly under extreme conditions.

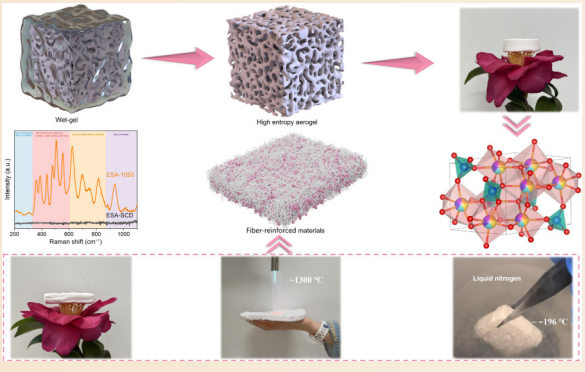

KEYWORDS: high entropy; ceramic aerogel; thermal stability; thermal insulation

1 Introduction

The use of high-performance ceramic materials is becoming increasingly widespread across various applications, including but not limited to the aerospace industry, electronics, and energy sectors. These materials primarily consist of carbides, oxides, borides, and nitrides. Nonoxide ceramics such as silicon carbide (SiC) and silicon nitride (Si_3N_4) offer several advantages, including high melting points, good thermal shock resistance, and excellent high-temperature strength. However, they are easily oxidized in a high-temperature oxygen atmosphere, which greatly reduces engine reliability and shortens their service life.

Oxide ceramics are among the various types of high-performance ceramic materials. They possess intrinsic antioxidant properties and exceptional mechanical strength at elevated temperatures, which has led to their rapid emergence as a focal point of research among scholars both domestically and internationally [1,2]. To further decrease the thermal conductivity and improve structural stability, the concept of high entropy has been introduced into ceramic systems. Compared with other oxide ceramics, high-entropy silicate ceramics have excellent high-temperature resistance, low thermal conductivity, and corrosion resistance [3]. Moreover, in comparison with conventional rare-earth silicates, high-entropy rare-earth silicates have significant advantages. From a thermodynamic perspective, the coexistence of multiple rare-earth cations increases the configurational entropy (ΔS_{conf}), thereby lowering the Gibbs free energy ($\Delta G = \Delta H - T\Delta S_{conf}$, where ΔH is the enthalpy term, and T is the absolute temperature) and stabilizing the disordered solid solution phase at high temperatures. This process of entropy-driven stabilization

[1] State Key Laboratory of Materials-Oriented Chemical Engineering, College of Materials Science and Engineering, Nanjing Tech University, Nanjing 211816, China. [2] Jiangsu Collaborative Innovation Center for Advanced Inorganic Function Composites, Nanjing 211816, China.

✉ Corresponding authors. E-mail: J. Yang, yangjian1976@163.com; S. Cui, scui@njtech.edu.cn

Received: June 15, 2025; Revised: October 18, 2025; Accepted: November 25, 2025

has been shown to suppress the crystallization and phase decomposition that are commonly observed in single-component silicates [4]. From a kinetic standpoint, the lattice distortion and local chemical disorder induced by multication mixing significantly increase the atomic diffusion barriers, thereby inhibiting grain growth and sintering during thermal treatment. Furthermore, the fluctuations in mass and strain fields caused by cations with different sizes and atomic masses enhance phonon scattering, thereby reducing the lattice thermal conductivity [5]. Collectively, high-entropy rare-earth silicates demonstrate superior structural stability and thermal insulation performance at elevated temperatures.

For example, Chen *et al.* [6] synthesized $(Ho_{0.25}Lu_{0.25}Yb_{0.25}Eu_{0.25})_2SiO_5$ powder via a solid-phase sintering process with metal oxides as raw materials. This powder exhibited a low thermal conductivity of only 1.47 W/(m·K) at 800 °C, which was 26% lower than that of the monosilicates. However, calcination at 1550 °C for 12 h is required for preparation, resulting in high energy consumption. Thus, Liu *et al.* [7] employed molten-salt synthesis to prepare $(Y_{0.2}Sm_{0.2}Eu_{0.2}Er_{0.2}Yb_{0.2})_2SiO_5$, achieving a thermal conductivity of 0.96 W/(m·K) at 1000 °C while reducing the formation temperature of the high-entropy pure phase to 1400 °C for 4 h. Wei *et al.* [8] also used a chemical coprecipitation method instead of a high-temperature solid-phase sintering method and explored the use of high-entropy rare-earth monosilicate and bisilicate powders at various calcination temperatures. They were able to prepare high-entropy phases by calcining the powders at 1100 °C for only 2 h. However, they did not explore the performance of the resulting samples.

Aerogels possess ultralow density and thermal conductivity [9–11]. Integrating the high-entropy concept into ceramic aerogels can provide materials that simultaneously exhibit outstanding thermal insulation and enhanced structural stability at high temperatures. For example, Liu *et al.* [12] employed the sol–gel method to prepare $(LaCeSmEuNd)_2Zr_2O_7$ ceramic aerogels, achieving a room-temperature thermal conductivity of 0.073 W/(m·K) in a pressed aerogel. Wang *et al.* [13] prepared a ceramic aerogel with the composition $(La_{1/4}Sm_{1/4}Gd_{1/4}Y_{1/4})_2Zr_2O_7$ via the electrostatic spinning method. This material exhibited an ultralow thermal conductivity of only 0.082 W/(m·K) at 1000 °C, along with excellent thermomechanical stability. Han *et al.* [14] prepared $(La_{0.2}Y_{0.2}Sm_{0.2}Eu_{0.2}Nd_{0.2})_2Zr_2O_7$ ceramic aerogels via silane modification on the basis of a preparation method developed by previous researchers. The introduction of silica led to a partial transformation of the defective fluorite structure formed after calcination into a pyrochlore crystal structure, thereby enhancing the aerogel's high-temperature thermal stability. Furthermore, compared with that of the unmodified high-entropy ceramic aerogel, the thermal conductivity at room temperature decreased from 0.139 to 0.065 W/(m·K). However, conventional ceramic aerogels fail to meet the application requirements for thermal insulation systems [15–17]. The inherent brittleness of ceramic aerogels can be enhanced through the integration of continuous structural units. For example, polymer-crosslinked ceramic composite aerogels and fiber-reinforced ceramic aerogels have been used [18–21].

Therefore, in our previous research, we prepared Yb_2SiO_5 and $(YErYbLu)_2SiO_5$ ceramic aerogels to investigate the high-temperature stability and mechanical properties of single-element and quaternary silicate ceramic aerogels, respectively. The mechanical properties of pure silicate aerogels are suboptimal because of their inadequate temperature resistance. On the basis of our original work, we proceeded to fabricate five-membered high-entropy silicate ceramic aerogels by employing formamide, a templating agent characterized by shorter molecular chains. The high-entropy ceramic aerogels obtained prior to and following heat treatment were found to be intact blocks and did not collapse or sinter at 1600 °C for 2 h, exhibiting enhanced high-temperature phase stability and thermal stability. In this study, the high-temperature thermal stability and thermal insulation properties of various fiber-reinforced materials are examined after 2 h of annealing at different temperatures. Furthermore, the improvement effect on the mechanical and thermal properties is investigated.

2 Experimental

2.1 Materials

The experiments involved rare-earths: $RECl_3{\cdot}6H_2O$ (RE = Y, Yb, Gd, Dy, and Er) (99.9%, Shanghai Macklin Biochemical Co., Ltd., China,); reagents: tetraethyl orthosilicate (TEOS; 99.7%, Shanghai Macklin Biochemical Co., Ltd., China), formamide ($HCONH_2$; 99.7%, Shanghai Macklin Biochemical Co., Ltd., China), ethanol (EtOH; 99.7%, Sinopharm Chemical Reagent Co., Ltd., China), 1,2-propylene oxide (PO; 99.5%, Shanghai Macklin Biochemical Co., Ltd., China); and deionized water (H_2O; Nanjing Wanqing Chemical Glass Instrument Co., Ltd., China). The fiber-reinforced materials were purchased from Zhejiang Oka Refractory Materials Co., Ltd., China (density: 0.104–0.123 g/cm^3; fiber diameter: 3–10 μm; thermal conductivity: 0.034–0.042 W/(m·K)).

2.2 Fabrication of $YYbErDyGd)_2SiO_5$ ceramic aerogels

Figure 1(a) illustrates the experimental preparation steps. Initially, five metal salts (2 mmol of each metal salt) were dissolved in 0.5 mol of EtOH and 0.3 mol of H_2O, and the solution was stirred until salts were fully dissolved. Subsequently, 10 mmol of CH_3NO was added to the aforementioned solution, and then the resulted solution was stirred for 20 min. Separately, 20 mmol of TEOS was added, followed by stirring for 30 min. Thereafter, 80 mmol of PO was added, followed by stirring for 30 s. The resulting mixture was quickly transferred into a custom mold. Then, the precursor wet gel was obtained. After aging for 6 h, the EtOH solution was replaced four times (each replacement lasted 6 h). Finally, the high-entropy aerogel precursor was obtained after CO_2 supercritical drying (SCD). Afterwards, the precursors were calcined at 950, 1050, 1250, and 1350 °C in an air atmosphere for 2 h, thereby yielding high-entropy silicate aerogels (ESA-*t*, *t* denoting the temperature). A pure X1-phase $(YYbErDyGd)_2SiO_5$ ceramic aerogel was synthesized at 1050 °C. For subsequent tests, ESA-1050 was air annealed at 1000–1600 °C for 2 h (named RESA-*t*) to analyze the phase stability and pore structure of the pure aerogel.

2.3 Fabrication of fiber-reinforced high-entropy ceramic aerogels

The fabrication of fiber-reinforced high-entropy ceramic aerogels was conducted in accordance with the previously outlined procedure. The process involved the initial addition of PO, followed by the pouring of the mixture into the designated molds. The molds were then replaced with pre-cut fiber mats measuring 30 mm × 30 mm × 10 mm. The samples subsequently underwent the same aging, EtOH substitution, and SCD processes as previously described. The final step involved calcination for 2 h in air at 1050 °C, which resulted in the production of four fiber-

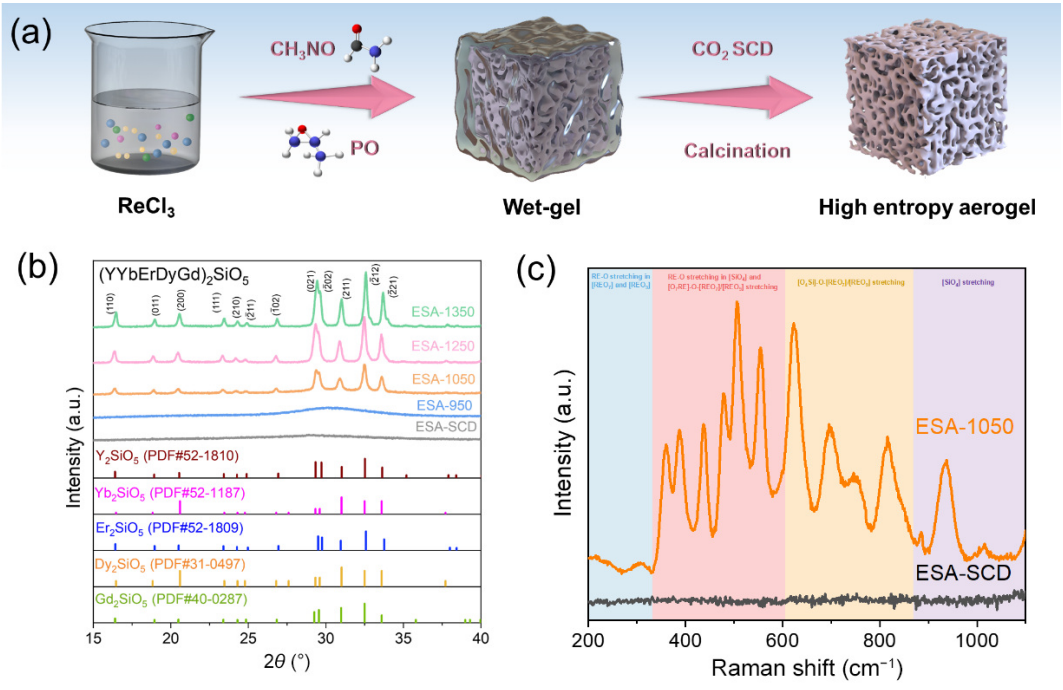

Fig. 1 (a) Schematic illustration of preparation of ESAs. (b) XRD patterns of ESAs at different sintering temperatures. (c) Raman spectra of ESA-SCD and ESA-1050.

reinforced high-entropy ceramic aerogel materials: silicate fiber cotton (XFESA), silicate fiber felt (GFESA), mullite fiber (MFESA), and polycrystalline mullite fiber (DFESA)-reinforced ceramic aerogels. The aerogel solid content of the fiber-reinforced aerogel was calculated to be 38.5±1.5 wt% according to Eq. (1).

$$\text{Aerogel solid content (wt\%)} = \frac{m_{\text{composite}} - m_{\text{fiber}}}{m_{\text{composite}}} \times 100\% \quad (1)$$

where $m_{\text{composite}}$ and m_{fiber} denote the masses of the fiber-reinforced high-entropy ceramic aerogel and pure fiber, respectively.

2.4 Characterization and measurements

An Ultima IV instrument was used to record X-ray diffraction (XRD) patterns with Cu Kα radiation (λ = 0.15406 nm) at a scan rate of 10°/min. Fourier transform infrared (FTIR) spectroscopy was implemented with a Perkin-Elmer Spectrum GX to study the chemical groups of the samples. Aerogels were collected at wavelengths ranging from 200 to 1100 cm^{-1} via an Evolution Raman spectrometer (Thermo Fischer DXR, USA). A scanning electron microscope (SEM; Supra55, Zeiss, USA) was used to obtain microstructural images of all the aerogels. An energy-dispersive X-ray spectrometer (EDS) connected to the SEM was used for elemental mapping. A transmission electron microscope (TEM; JEM 2100F, JEOL, Japan) was used to determine the crystal structure of the aerogel. A Micromeritics ASAP020 instrument was used to measure the Brunauer–Emmett–Teller (BET) specific surface area and pore diameter of the aerogels. Mercury intrusion porosimeter (MIP) was performed via AutoPore Iv 9510. A NETZSCH STA 449F3A instrument was used to obtain thermogravimetric analysis (TG) and differential scanning calorimetry (DSC) curves, which were used to test the ceramic aerogel precursor from room temperature to 1500 °C (heating rate of 10 °C/min) in an oxygen atmosphere. The insulation properties of the high-entropy aerogel were determined with a DRPL-III thermal conductivity meter, and the tested sample size was 30 mm × 30 mm × 10 mm. The thermal conductivity test described above was averaged after three tests for each sample. The compressive strength of the aerogel sample was calculated via an electric universal testing machine (CMT6103) with a displacement rate of 0.5 mm/min. Following YB/T 4130-2005, the high-temperature thermal conductivity of the fiber-reinforced materials was measured via a PBD-12-4P thermal conductivity tester (diameter of 180 mm and thickness of 10 mm).

Equation (2) was used to calculate the density, where ρ is the density of the aerogel, m is the mass of the aerogel, and V is the volume of the aerogel.

$$\rho = \frac{m}{V} \quad (2)$$

Equation (3) was used to calculate the porosity, where P is the porosity of the aerogel, ρ is the density of the aerogel, and ρ_0 is the apparent density.

$$P = \left(1 - \frac{\rho}{\rho_0}\right) \times 100\% \quad (3)$$

Equation (4) was used to calculate the compressive strength, where P_{max} is the maximum compressive strength of the aerogel, F_{max} is the maximum force, and A is the stressed area. The tested sample size was 30 mm × 30 mm × 10 mm.

$$P_{\text{max}} = \frac{F_{\text{max}}}{A} \quad (4)$$

Equation (5) was used to calculate the linear shrinkage, where S is the linear shrinkage of the aerogel and L_0 and L_1 are the sizes before and after calcination, respectively.

$$S = \frac{L_0 - L_1}{L_0} \times 100\% \quad (5)$$

3 Results

3.1 Phase composition of ESA

Figure 1(b) shows the XRD patterns of the ESA precursors after calcination at different temperatures for 2 h, along with the physical phase composition of the synthesized five-component

equimolar ESA ceramic aerogels. However, the lower temperature is insufficient to provide sufficient driving force and energy for the complete solid solution reaction. Consequently, the high-entropy ceramic aerogel precursor manifests as an amorphous bun peak before calcination at 1050 °C (Fig. 1(b)). This observation signifies that the high-entropy formation temperature is within the range of 950–1050 °C. The twelve characteristic peaks present at positions of approximately 16.4°, 18.9°, 20.5°, 23.4°, 24.3°, 24.9°, 26.8°, 29.4°, 29.5°, 31.0°, 32.4°, and 33.7°, which correspond to the (110), (011), (200), (111), (210), ($\bar{2}$11), ($\bar{1}$02), (021), ($\bar{2}$02), (211), ($\bar{2}$12), and ($\bar{2}$21) crystallographic planes, respectively. These peaks were analyzed by comparison with a five-component standard PDF card, which matched the characteristic peaks of the monosilicate X1 phase (X1-RE_2SiO_5), and no other impurities were detected, indicating the formation of a single-phase structure. Furthermore, an increase in the calcination temperature from 950 to 1350 °C resulted in a sharpening of the characteristic peaks of the high-entropy ceramic aerogels.

To further confirm that the synthesized $(YYbErDyGd)_2SiO_5$ ceramic aerogel has an X1-RE_2SiO_5 crystal structure, Fig. 1(c) presents the Raman spectra before and after calcination, which are primarily divided into four regions of characteristic peaks. The Raman shift range of 200–332 cm^{-1} is associated with the displacement of the metal ion RE, leading to the stretching vibrations of the [REO_7] and [REO_9] groups. The majority of the characteristic peaks are located in the second region, spanning 332–605 cm^{-1}, which corresponds to the vibrations of the two atoms, Si and RE. These vibrations are attributed to the RE–O–RE stretching between the [REO_7] and [REO_9] groups present in X1-RE_2SiO_5 [22,23], as well as to the bending vibrational peaks of the Si–O bonds in the [SiO_4] group. The three prominent characteristic peaks observed in the range of 605–868 cm^{-1} are attributed to the bending vibrations of the [SiO_4] group, whereas the peak in the range of 868–1100 cm^{-1} corresponds to the stretching vibrations of the [SiO_4] group [8].

XPS analysis was conducted on the ESA-1050 sample to determine the elemental composition of the ESA materials and the formation of oxygen vacancies. As shown in Fig. 2(a), all the XPS peaks calibrated with C 1s indicate signals from Y, Yb, Er, Dy, Gd, Si, and O elements. In Fig. 2(b), the Y 3d spectrum displays two main peaks attributed to the Y $3d_{3/2}$ and Y $3d_{5/2}$ orbitals, located at 159.16 and 157.03 eV, respectively. The peaks

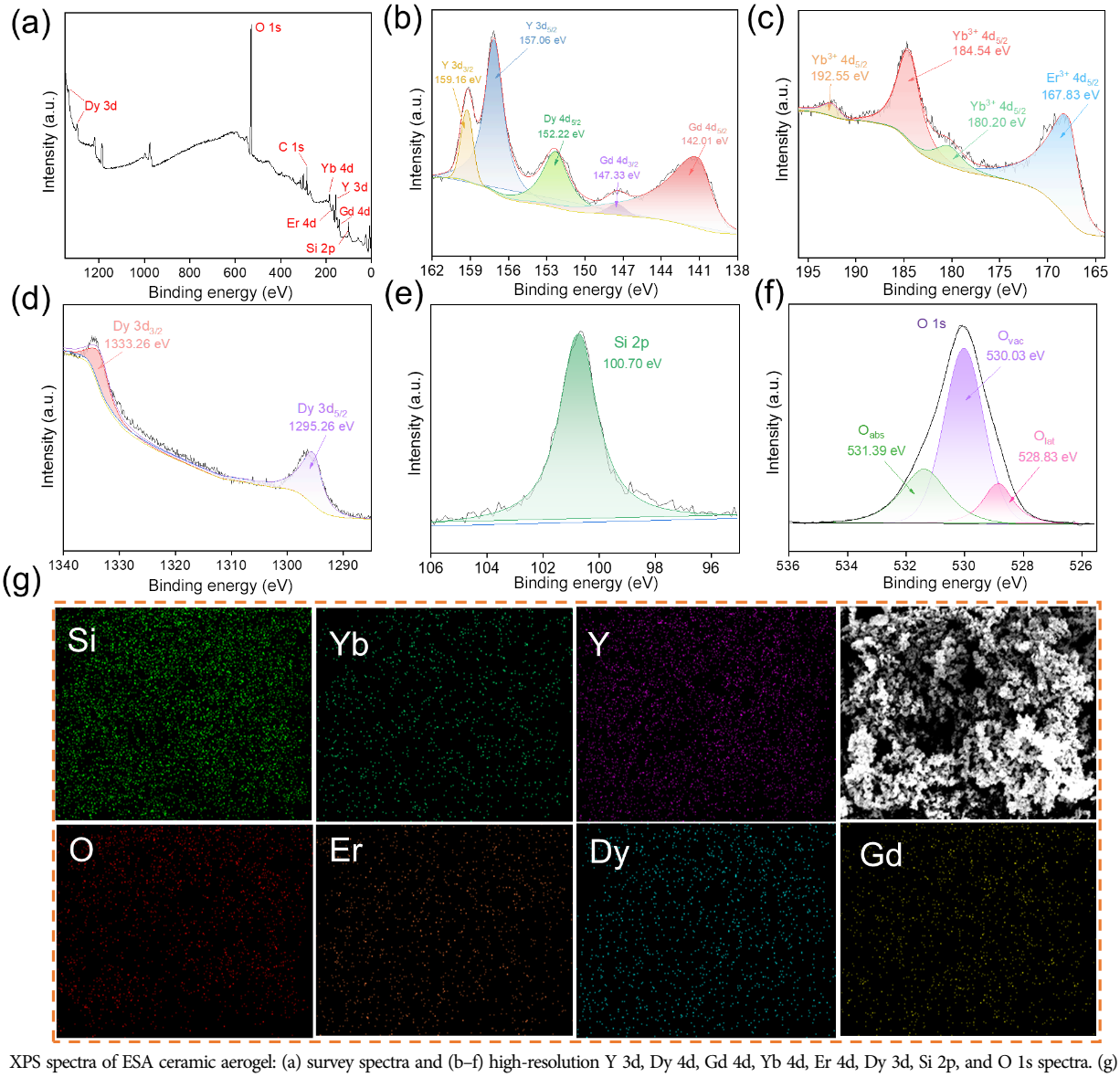

Fig. 2 XPS spectra of ESA ceramic aerogel: (a) survey spectra and (b–f) high-resolution Y 3d, Dy 4d, Gd 4d, Yb 4d, Er 4d, Dy 3d, Si 2p, and O 1s spectra. (g) EDS elemental mappings of ESAs.

at 147.33 and 142.01 eV are associated with Gd^{3+} [24]. According to Fig. 2(c), the Yb 4d spectrum can be fitted into three peaks located at 192.55, 184.54, and 180.20 eV, which are assigned to Yb $4d_{5/2}$, whereas an additional peak corresponds to Er $4d_{5/2}$ [25]. The Dy 3d spectra shown in Fig. 2(d) exhibit two peaks at 1333.26 and 1295.26 eV. In Fig. 2(e), the position of the binding peak at 100.70 eV corresponds to the binding energy spectrum of Si 2p [26]. As illustrated in Fig. 2(f), the O 1s spectrum reveals three notable peaks. The peaks at 528.83, 530.03, and 531.39 eV are attributed to lattice oxygen, oxygen vacancies, and chemisorbed oxygen, respectively, with a dominant presence of oxygen vacancies [27]. The compositional distribution of ESAs, as displayed in Fig. 2(g), confirms the presence of several elements (Y, Yb, Er, Dy, and Gd).

Figure 3(a) presents the infrared spectrograms recorded at different calcination temperatures. The ceramic aerogel precursor ESA-SCD exhibits a peak in the range of 3100–3600 cm^{-1}, which corresponds to the O–H stretching vibration. This peak indicates the presence of adsorbed water and residual ethanol within the pore structure of the aerogel. The peak associated with the O–H stretching vibration disappears after calcination at 950 °C for 2 h, indicating the effective removal of adsorbed species. Additionally, the stretching vibration peak observed at 1385 cm^{-1} is attributed to the C–O bond found in the organic matter present in the ceramic aerogel precursor. As the calcination temperature increases, this peak gradually diminishes, ultimately indicating the complete decomposition of the organic matter in the air. This process enhances the structural integrity and purity of the resulting ceramic aerogel. In addition, several characteristic peaks of the monosilicate structure emerged after calcination at 1050 °C for 2 h. Specifically, the peak at 1019 cm^{-1} is associated with the tensile vibration of the RE–O–RE bond. The peak at 873 cm^{-1} corresponds to the tensile vibration of Si–O–Si within SiO_4. Furthermore, the peaks at 550 and 489 cm^{-1} correspond to the stretching and bending vibrations of the RE–O bond in the REO_7 ligand of the X1-RE_2SiO_5 structure, respectively [28].

Figure 3(b) presents the thermogravimetric curves and the corresponding DSC curves of ESA-SCD in an air atmosphere. The observed processes can be divided into three distinct stages. In the first stage, a heat absorption peak appears at 146.5 °C, occurring within the temperature range of room temperature to 233.5 °C, and is attributed to the removal of physically adsorbed H_2O and residual EtOH from the pore structure of the aerogel precursor, contributing to a weight loss of 6.28%. In the second stage, an exothermic peak is observed at 342.4 °C within the temperature range of 233.5–871.2 °C [29]. The broader exothermic peak is related to the condensations of hydroxyl and alkoxyl groups, along with the concomitant removal of strongly bound water molecules, resulting in an approximate weight reduction of 19.83% during this stage. Within the higher temperature range of 871.2–1500 °C, a sharper heat absorption peak is subsequently observed at 1040.0 °C. However, no significant weight loss occurs at this temperature, which corresponds to the formation of a $(YYbErDyGd)_2SiO_5$ phase that includes five oxides [30]. The appearance of these peaks confirms the formation of the monosilicate structure, indicating successful structural development during the calcination process. When the temperature was increased to 1350 °C, a partial crystalline transition may have occurred because of the excessively high temperature.

TEM was used to analyze the crystal structure and elemental distribution of the high-entropy aerogel (Fig. 4). High-resolution TEM (HRTEM) images and selected area electron diffraction (SAED) patterns presented in Figs. 4(a) and 4(b) were obtained from the red-marked areas. The HRTEM refinement results indicate that the measured crystal spacings of 0.330, 0.277, 0.540, and 0.288 nm correspond to the (021), ($\bar{2}$12), (110), and (211) crystal planes, respectively. These findings are consistent with the lattice constants of the high-entropy aerogel calculated from the XRD data, according to Eq. (6) ($a = 9.011$, $b = 6.952$, $c = 6.634$) [31].

$$\frac{1}{d_{hkl}^2} = \frac{h^2}{a^2} + \frac{k^2\sin^2\beta}{b^2} + \frac{l^2}{c^2} - \frac{2hl\cos\beta}{ac} \tag{6}$$

where d_{hkl} is the interplanar spacing of the (hkl) lattice planes; h, k, and l are the Miller indices corresponding to the crystallographic plane; a, b, and c represent the lattice parameters of the unit cell along the crystallographic axes; β denotes the angle between the a- and c-axes in the monoclinic crystal system.

The absence of other crystal structures in the TEM images of ESA-1050 indicates the formation of a pure-phase crystal structure that has strong solid solution properties and high crystallinity. Consequently, the aerogel precursor can be transformed into a single-phase high-entropy ceramic aerogel through heating at temperatures up to 1050 °C, which corresponds to the crystalline transition temperature analyzed via TG–DSC. Furthermore, the inverse Fourier transform (IFFT) map of the area highlighted by the yellow squares in Fig. 4(b) corroborates the presence of dislocations in the nonisomorphic high-entropy phase, as indicated by the "T" symbol. This phenomenon can be attributed to imperfect orientation during the formation of the high-entropy single phase, along with crystal growth resulting from significant lattice distortions and vacancy aggregation induced by high-entropy effects [32]. Importantly, HRTEM identification provides a more comprehensive overview of the crystal surface because of

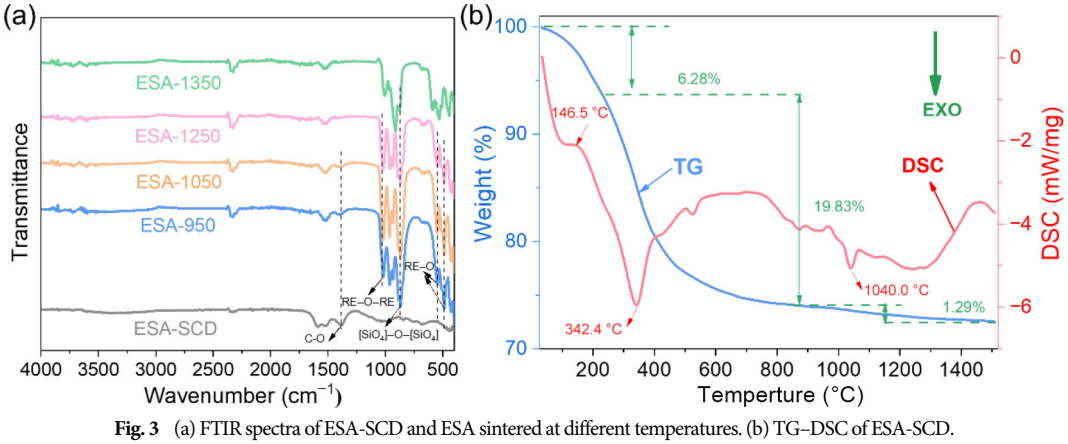

Fig. 3 (a) FTIR spectra of ESA-SCD and ESA sintered at different temperatures. (b) TG–DSC of ESA-SCD.

清華大学出版社 Tsinghua University Press | SciOpen

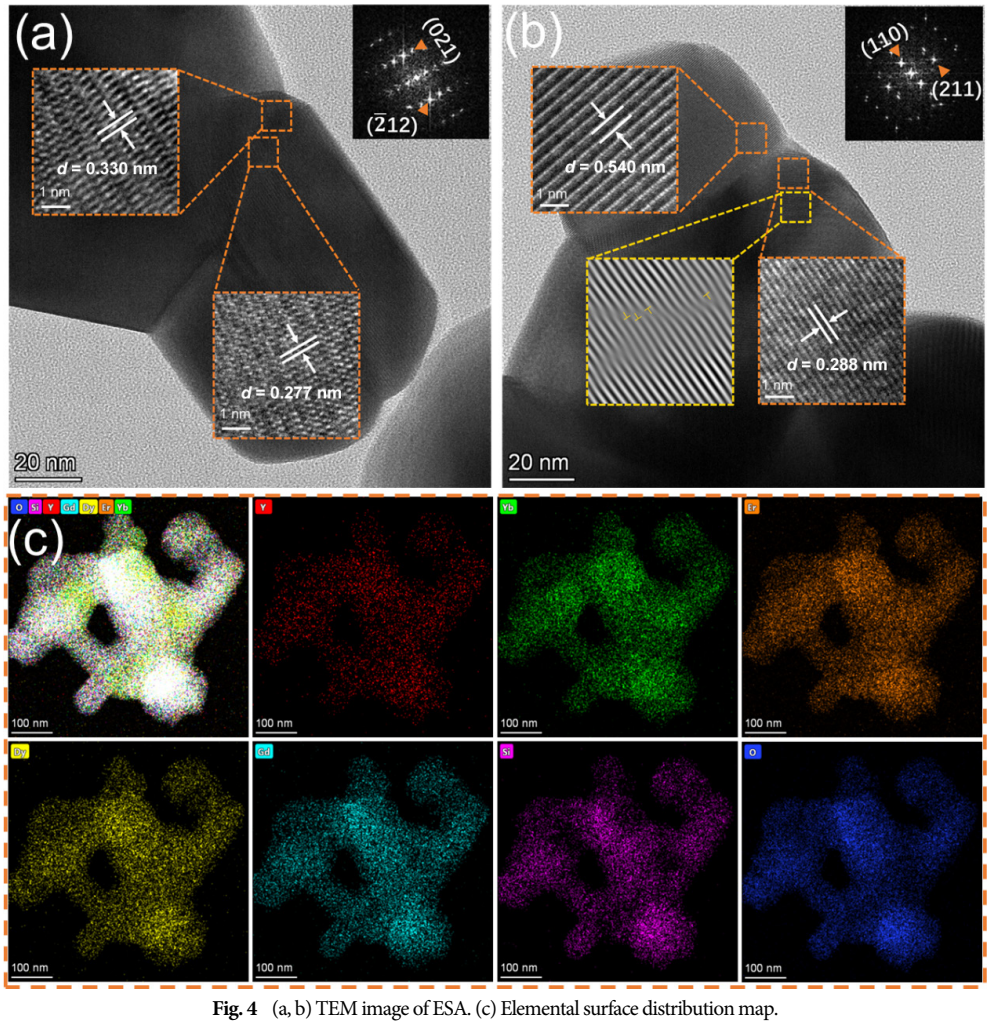

Fig. 4 (a, b) TEM image of ESA. (c) Elemental surface distribution map.

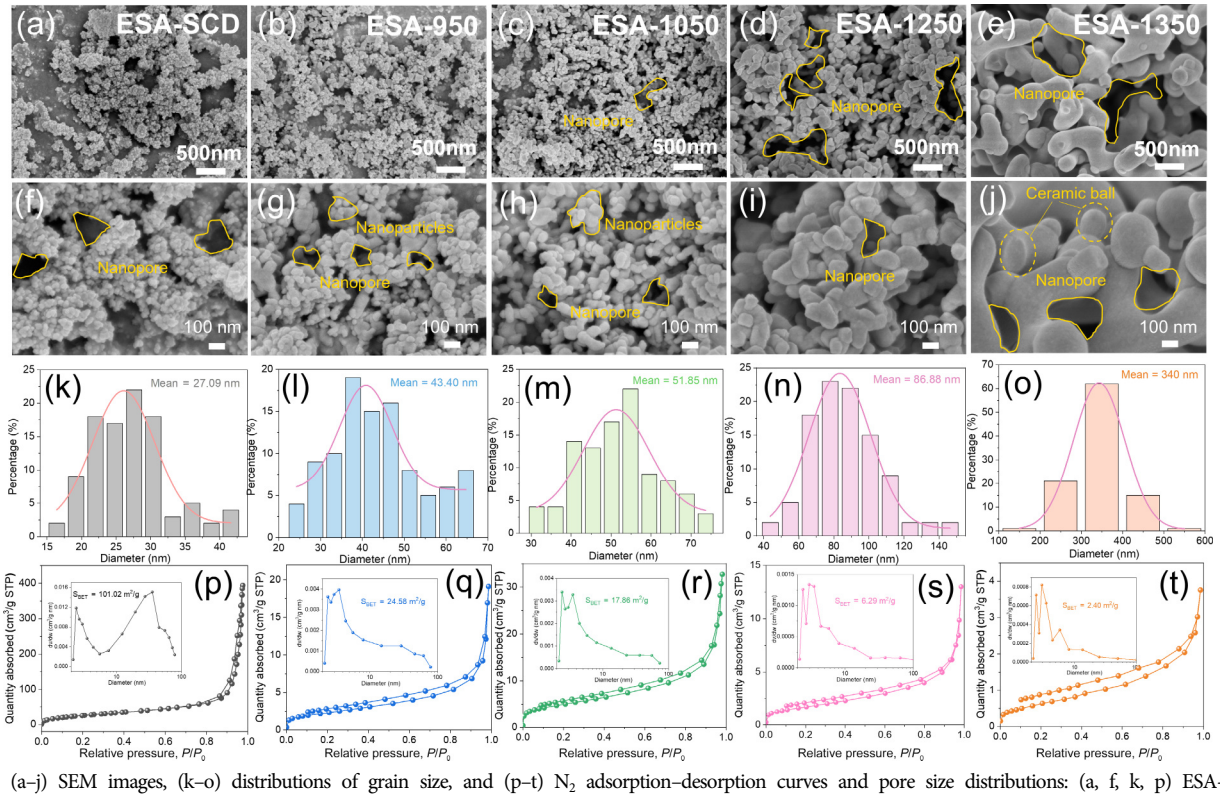

Fig. 5 (a–j) SEM images, (k–o) distributions of grain size, and (p–t) N_2 adsorption–desorption curves and pore size distributions: (a, f, k, p) ESA-SCD; (b, g, l, q) ESA-950; (c, h, m, r) ESA-1050; (d, i, n, s) ESA-1250; (e, j, o, t) ESA-1350.

its superior sensitivity compared with that of XRD analysis [33]. EDS mapping (Fig. 4(c)) further confirms the uniform spatial distribution of substitutional cations at the grain scale, with no visible segregation [34].

3.2 Microstructure of ESA

SEM analysis was conducted on samples that had undergone calcination at temperatures ranging from 950 to 1350 °C for 2 h. Figures 5(a)–5(j) shows the microstructures at different magnifications. As shown in Figs. 5(a) and 5(f), the ESA-SCD aerogel exhibits a characteristic three-dimensional (3D) nanoporous network structure consisting of nanoparticles and nanopores, along with a limited number of macropores. The pore size ranges from 20 to 50 nm, with an average particle size of 27.09 nm (Figs. 5(k) and 5(p)). Notably, after calcination at 1050 °C for 2 h, the pore size distribution becomes significantly more homogeneous. This homogeneity is attributed to the decomposition of formamide during the calcination process in an oxygen atmosphere. As the calcination temperature increases, the high chemical potential of the particle surfaces and the low chemical potential at the necks lead to intensified surface diffusion among the particles, promoting neck formation. As a result, the aerogel skeleton gradually thickens, resulting in a decrease in specific surface area and a reduction in pore size [35]. As illustrated in Figs. 5(k)–5(o), the grain size distribution of ESAs significantly increases in size, increasing from 51.85 to 86.88 nm as the temperature increases from 1050 to 1250 °C. Figures 5(r)–5(t) reveals a significant increase in the number of large pores, which helps reduce the thermal conductivity of the material. However, there is no notable change in the pore distribution with varying temperatures. When the temperature reaches 1350 °C, the particle size of the ESA-1350 sample increases significantly to 340 nm. Interestingly, nanoceramic spheres developed on these particles, and varying particle shapes can influence the pore size distribution [36].

The N_2 adsorption isotherms and Barrett–Joyner–Halenda (BJH) pore size distributions of the composite aerogels treated at different heat treatment temperatures are illustrated in Figs. 5(p)–5(t). According to the IUPAC classification, the adsorption isotherms fall under a mixture of type II and type IV, exhibiting H3 hysteresis loops [37,38]. The BJH pore size distribution for the ESA-SCD samples shows two peaks in the range of 2–60 nm, indicating an inhomogeneous pore structure. The specific surface area of ESA-SCD is 101.02 m^2/g. With increasing temperature, the specific surface area gradually decreases. However, BET analysis can measure and calculate only pore sizes that are smaller than 170 nm [39]. The specific pore structure values for the samples are provided in Table 1. The porosity of the sample was calculated via Eq. (3). Concurrently, with increasing calcination temperature, the porosity gradually decreases but remains above 70.48% throughout the process. Notably, the average pore sizes presented do not account for all the pores within the aerogel matrix owing to the limitations of the N_2 adsorption method. As the treatment temperature increases, a partial collapse of the mesopores has been observed, resulting in a decrease in pore volume.

3.3 High-temperature stability of ESA

3.3.1 *High-temperature phase stability*

To evaluate the high-temperature thermal stability and phase stability of the high-entropy ceramic aerogel, the sample ESA-1050 was subjected to an annealing thermal assessment at temperatures ranging from 1200 to 1600 °C in an air atmosphere for 2 h. The resulting XRD patterns are shown in Fig. 6. The phase of RESA-1200 remains X1-RE_2SiO_5. At 1300 °C for 2 h, a transition occurs to the X2-RE_2SiO_5 phase, which persists until 1600 °C for 2 h [6,40,41]. However, at temperatures between 1300 and 1600 °C, the local magnification of the XRD patterns clearly shows that the diffraction peaks shifted slightly to the left with increasing annealing temperature.

3.3.2 *High-temperature thermal stability of microstructure*

The RESA samples were further analyzed via SEM and BET tests to provide more detailed insight into the microstructure of the samples following the process of annealing. The results of the analysis, presented in Figs. 7(a)–7(j), demonstrate that the distribution of the RESA pore structure remained consistent as the

Table 1 Pore structure data of ESA-SCD and ESA samples

Sample	Average pore size (nm)	BJH absorption volume (cm^3/g)	Porosity (%)
ESA-SCD	24.12	0.62	—
ESA-950	11.80	0.07	75.77
ESA-1050	11.34	0.05	74.74
ESA-1250	12.78	0.02	72.24
ESA-1350	9.66	0.01	70.48

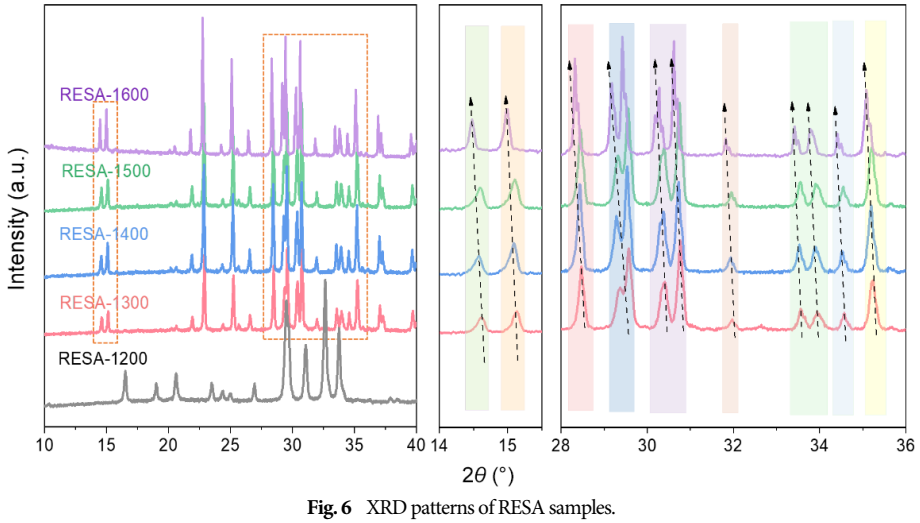

Fig. 6 XRD patterns of RESA samples.

temperature increased. However, the aerogel skeleton underwent a process of thickening due to the increase in temperature, resulting in a gradual increase in the size of the grains. No fusion or sintering occurred during this process. Interestingly, some ceramic spheres were observed on the surface of the grains in the high-magnification image (Figs. 7(g) and 7(h)) of the ESA-1050 sample after calcination at temperatures over 1300 °C for 2 h. This observation indicates that the aerogel particle skeleton gradually transforms into porous ceramics as the annealing temperature increases [36]. Moreover, Fig. 8 reveals that the Si signal intensity within the spherical regions of the RESA-1300 sample is markedly higher than that of the surrounding matrix, indicating the presence of localized silicon enrichment. This phenomenon may be associated with the formation of $RE_2Si_2O_7$ at elevated temperatures; the specific mechanism is discussed in detail in Section 4.2. As illustrated in Figs. 7(f)–7(j), the grain surface of the RESA-1600 sample appears to be more flattened and smoother than those of the other samples. This phenomenon is likely attributable to the elevated temperature, which results in local sintering of the nanograin, leading to a reduction in the surface roughness. As illustrated in Figs. 7(k)–7(o), the grain size of the RESA increases from 0.086 to 0.750 μm in direct proportion to the applied annealing temperature. This phenomenon can be observed in Figs. 7(p)–7(t), where it is evident that the specific surface area decreases with increasing temperature. The specific surface area of RESA-1600 is only 1.81 m^2/g, with a porosity of 62.55% and a pore volume (Table 2) approaching the characteristics of conventional porous ceramics. In accordance with the IUPAC classification, the adsorption isotherm is depicted as a mixture of type II and type IV compounds with an H3 hysteresis loop. This indicates that the structure is dominated by macropores at elevated temperatures.

3.4 Preparation and microstructure of fiber-reinforced high-entropy aerogel

In the context of elevated temperatures and complex environments, the mechanical properties of high-entropy ceramic aerogels have yet to be fully realized for direct utilization. To

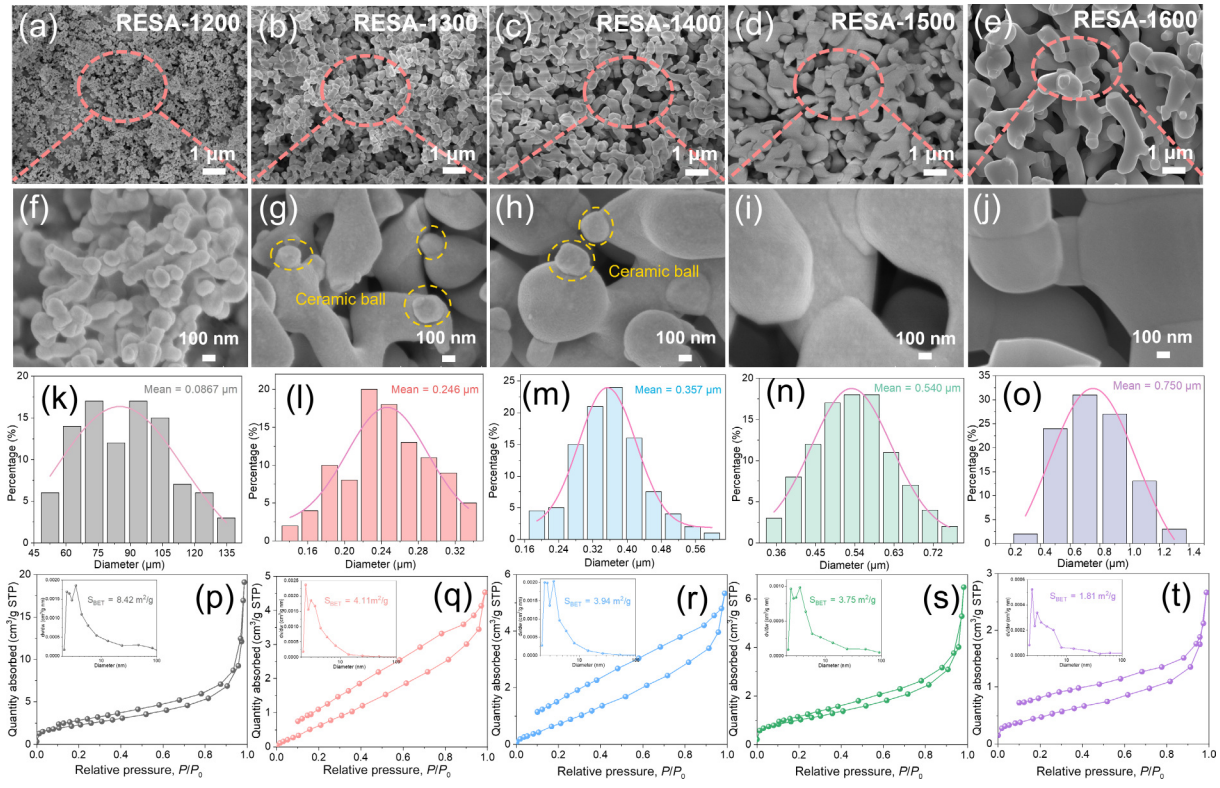

Fig. 7 (a–j) SEM images, (k–o) distributions of grain size, and (p–t) N_2 adsorption–desorption curves and pore size distributions: (a, f, k, p) RESA-1200; (b, g, l, q) RESA-1300; (c, h, m, r) RESA-1400; (d, i, n, s) RESA-1500; (e, j, o, t) RESA-1600.

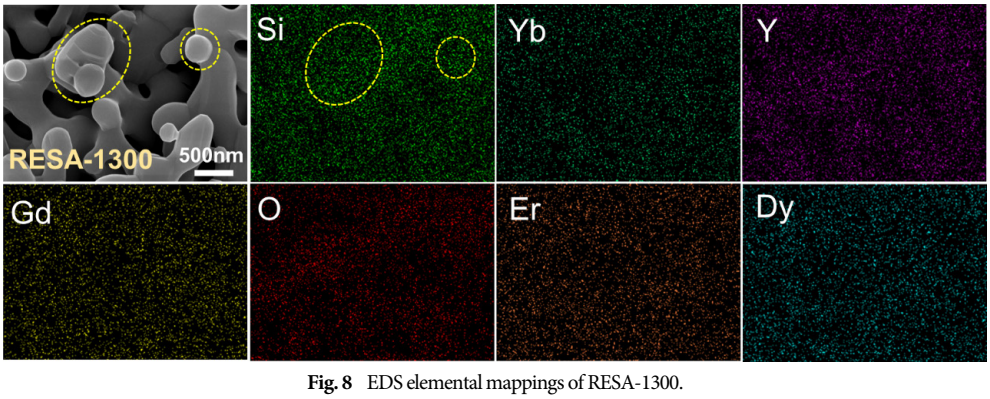

Fig. 8 EDS elemental mappings of RESA-1300.

enhance the mechanical properties of heat insulation materials, researchers typically employ fiber composite technology, a method that also facilitates the attainment of superior heat insulation characteristics [18]. Consequently, aluminosilicate and mullite fibers were selected to reinforce the high-entropy ceramic aerogel, as shown in Fig. 9(a). Moreover, the microscopic morphology of the fiber-reinforced high-entropy aerogels and their phase composition were explored. Furthermore, Figs. 9(b)–9(m) shows the SEM, N_2 adsorption–desorption curves, and pore size distributions of the fiber-reinforced aerogels after calcination at 1050 °C for 2 h. The predominant constituent of the fibers in the samples in Figs. 9(b), 9(f), 9(c), and 9(g) is aluminosilicate. The distinguishing factor between the two samples is the method of fiber knitting, which is evident through the comparison of local magnified images (Figs. 9(f) and 9(g)). The fibers in GFESA-1050 clearly exhibit a more regular arrangement. It is widely recognized that a regular weave is more effective at reducing slagging. However, it also leads to increased density and thermal conductivity of the material. To determine whether new phases formed in the fiber-reinforced material following high-temperature calcination, Fig. 10 displays the XRD patterns of various fiber-reinforced high-entropy aerogels. A comparison of the diffraction patterns with the PDF cards revealed that the diffraction peaks corresponded to X1-RE_2SiO_5 and mullite. No new substances were produced, confirming that the composite material is fundamentally physical in nature, with no chemical reactions occurring.

Research has shown that complex pore structures are more conducive to increased heat transfer processes, thereby lowering the thermal conductivity of the material and improving thermal insulation. The chemical composition of the fibers in the MFESA-1050 and DFESA-1050 samples is primarily composed of mullite, with the key difference being that the fiber crystal structure in DFESA-1050 is polycrystalline mullite. Although both samples have the same chemical composition, the performance of polycrystalline mullite can be optimized by adjusting the grain size

Table 2 Pore structure data of RESA samples

Sample	Average pore size (nm)	BJH absorption volume (cm^3/g)	Porosity (%)
RESA-1200	16.52	0.029	69.89
RESA-1300	12.46	0.011	68.72
RESA-1400	10.36	0.008	66.96
RESA-1500	7.29	0.007	64.46
RESA-1600	6.77	0.003	62.55

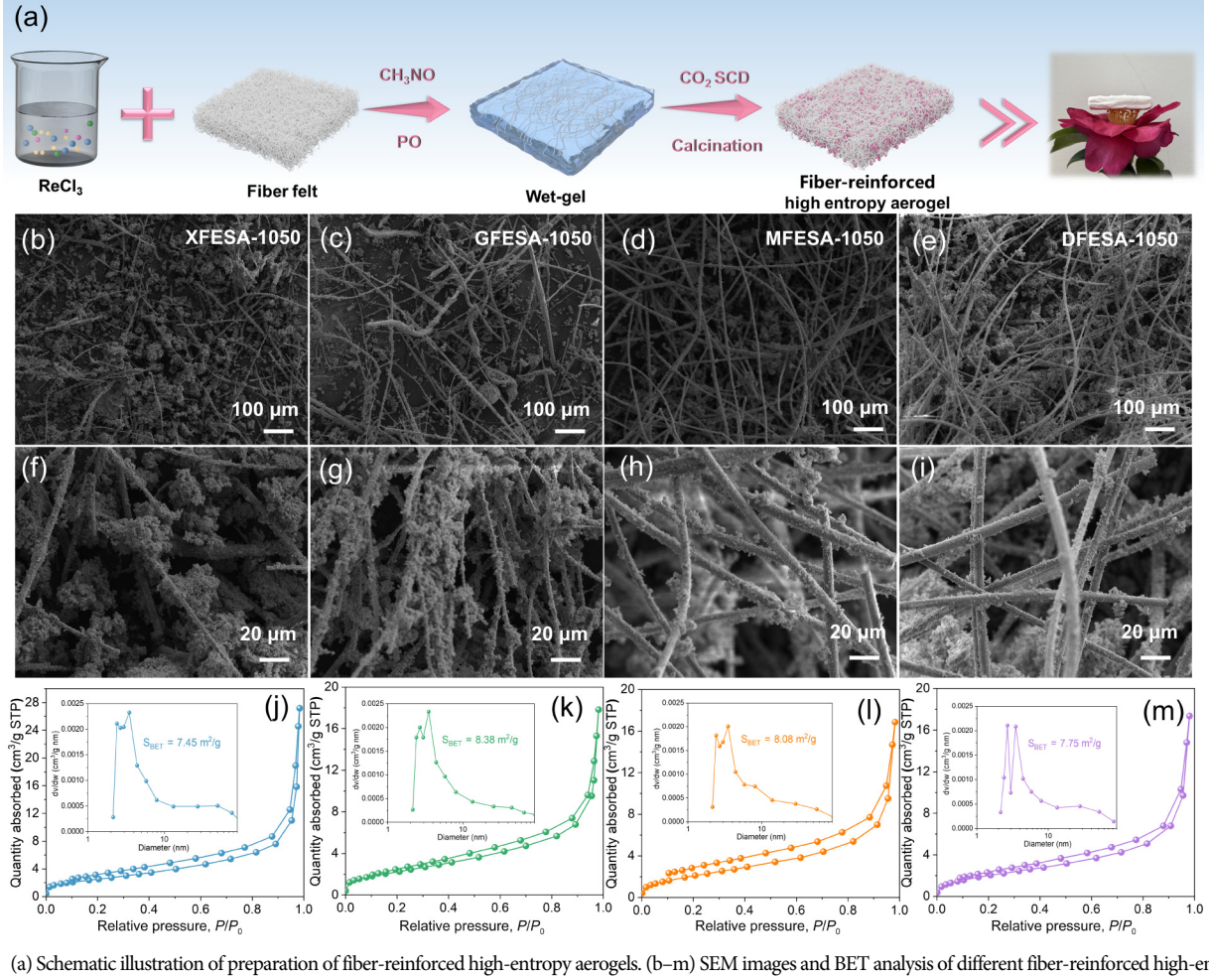

Fig. 9 (a) Schematic illustration of preparation of fiber-reinforced high-entropy aerogels. (b–m) SEM images and BET analysis of different fiber-reinforced high-entropy aerogels: (b, f, j) XFESA-1050; (c, g, k) GFESA-1050; (d, h, l) MFESA-1050; (e, i, m) DFESA-1050.

清華大学出版社 Tsinghua University Press | SciOpen

and sintering process, making it more suitable for industrial applications. Compared with silicate, mullite is a mineral produced from aluminosilicate at elevated temperatures. It possesses superior temperature resistance, which weakens the physical aging of the fibers during high-temperature calcination. Additionally, as seen from the SEM images, the fibers in the MFESA-1050 and DFESA-1050 materials are longer and more resilient, making them less prone to breakage at high temperatures. In addition, Figs. 9(j)–9(m) presents the N_2 adsorption–desorption curves, along with the pore size distributions for the four fiber-reinforced materials. The configuration of the hysteresis loop shape of the BET curve is predominantly attributable to the presence of micron-sized large pores. The specific surface areas of the four fiber-reinforced high-entropy aerogels ranged from 7.45 to 8.38 m^2/g. Compared with that of the RESA samples, a slight increase in the specific surface area is observed. An analysis of the findings in Table 3 clearly reveals that the incorporation of fiber mats exerts a negligible influence on the pore size distribution of the high-entropy ceramic aerogel (Figs. 5(p)–5(t)). The predominant form of the aerogel remains mesoporous and macroporous, a property that is more conducive to reducing the material's thermal conductivity.

3.5 Compressive strength of fiber-reinforced high-entropy aerogel

The fiber-reinforced high-entropy ceramic aerogel, obtained following calcination at 1050 °C for 2 h, underwent an annealing test at temperatures ranging from 1100 to 1300 °C for 2 h. The numerical variations in the density and shrinkage of the resulting samples are illustrated in Fig. 11(a). It is evident that MFESA exhibits the lowest density and line shrinkage of the four fiber reinforcements, with values of 0.208 g/cm^3 and 0.25%, respectively. Compared with the density of pure felt (Table 5), the overall density of the fiber-reinforced materials increased as a result of the incorporation of aerogel. The MIP results for the MFESA sample are shown in Fig. 11(b). The data indicate that the pore sizes are predominantly distributed within the 10–100 μm range, with two distinct peaks at approximately 0.1 and 20–30 μm, respectively. The corresponding pore structure parameters are summarized in Table 4. MFESA-1050 exhibits a relatively broader pore size distribution, which was mainly concentrated in the 10–30 μm range. The average pore size is 1.77 μm, and the porosity reaches a maximum of 92.76%, indicating a relatively loose skeletal structure. As the annealing temperature increases, both the specific surface area and porosity decrease, yet both remain above 83.11%. Figure 12 shows the compressive strength of the fiber-reinforced materials at different annealing temperatures. As the annealing temperature increases, the mechanical properties of the four different fiber-reinforced materials vary considerably. Following a 2-h examination at 1100 °C, GFESA exhibited the poorest mechanical properties, with a value of 0.109 MPa at 50% strain. Conversely, DFESA displayed the best mechanical properties, with a value of 0.368 MPa at 60% strain. As the annealing test temperature rises, the mechanical properties of GFESA and XFESA improve.

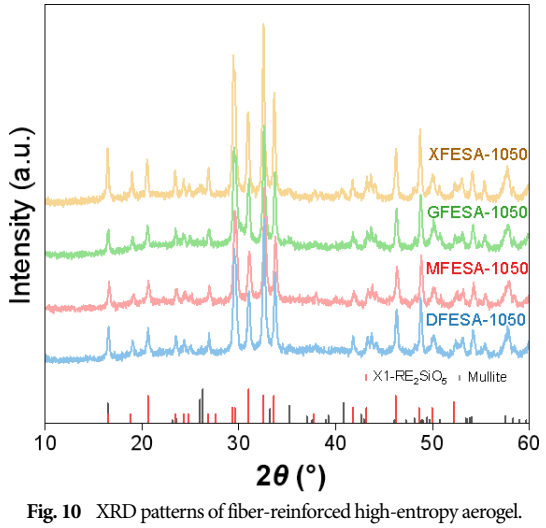

Fig. 10 XRD patterns of fiber-reinforced high-entropy aerogel.

3.6 High-temperature stability of fiber-reinforced high-entropy aerogels

3.6.1 *Thermal conductivity*

Figure 13(a) illustrates that the room temperature thermal conductivity of the four fiber-reinforced high-entropy ceramic

Table 3 Pore structure data obtained via BET method for fiber-reinforced high-entropy aerogel samples

Sample	Average pore size (nm)	BJH absorption volume (cm^3/g)
XFESA-1050	18.19	0.04
GFESA-1050	13.17	0.27
MFESA-1050	12.91	0.26
DFESA-1050	13.86	0.28

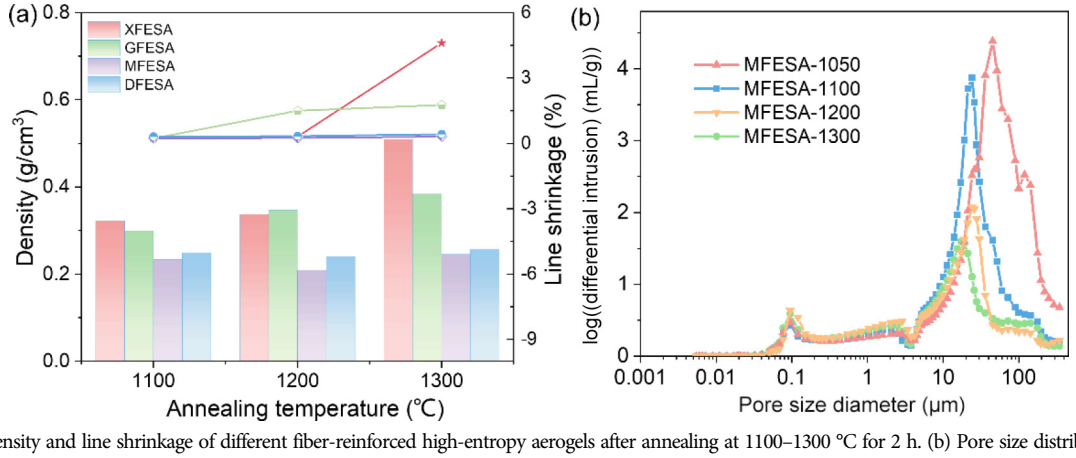

Fig. 11 (a) Density and line shrinkage of different fiber-reinforced high-entropy aerogels after annealing at 1100–1300 °C for 2 h. (b) Pore size distribution via MIP method of MFESA.

Table 4 Pore structure data obtained via MIP method for MFESA samples

Sample	Average pore size (μm)	Porosity (%)	S_{MIP} (m^2/g)
MFESA-1050	1.77	92.76	10.86
MFESA-1100	1.28	88.33	10.17
MFESA-1200	0.79	84.55	9.30
MFESA-1300	0.69	83.11	8.78

Table 5 Density and thermal conductivity of different pure fiber materials

Sample	Density (g/cm^3)	Thermal conductivity (W/(m·K))
Aluminosilicate fiber cotton	0.121	0.042
Aluminosilicate fiber	0.104	0.035
Mullite fiber	0.112	0.034
Polycrystalline mullite fiber	0.123	0.038

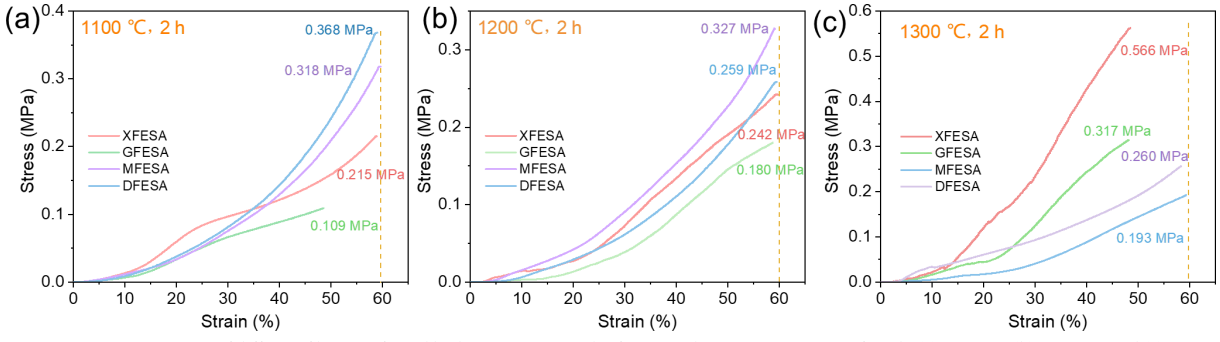

Fig. 12 Stress–strain curves of different fiber-reinforced high-entropy aerogels after annealing at 1100–1300 °C for 2 h: (a) 1100 °C, (b) 1200 °C, and (c) 1300 °C.

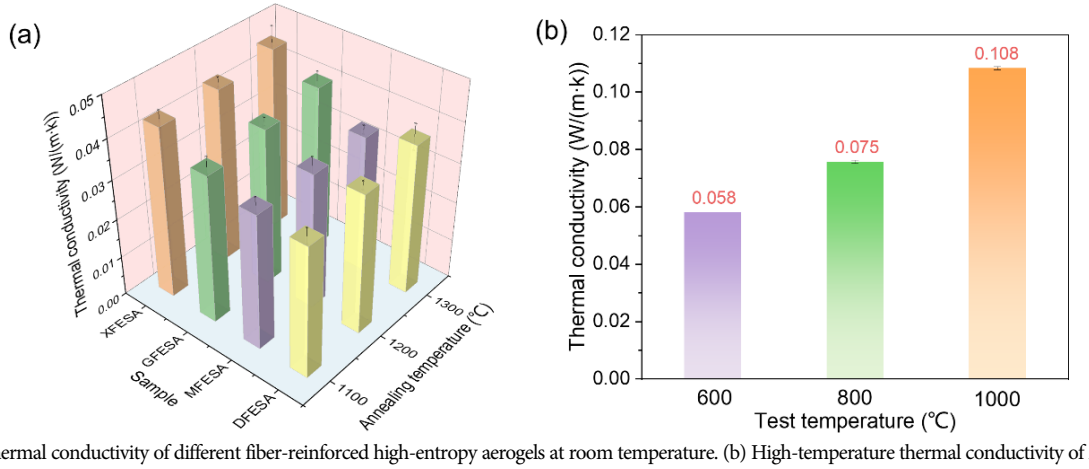

Fig. 13 (a) Thermal conductivity of different fiber-reinforced high-entropy aerogels at room temperature. (b) High-temperature thermal conductivity of MFESA-1050 sample.

aerogels tends to increase as the annealing temperature increases. Among them, MFESA has the lowest thermal conductivity of 0.032 W/(m·K) after annealing at 1100 °C for 2 h. The thermal conductivities of GFESA and XFESA are relatively high, which is highly related to the decrease in volume with increasing temperature and the increase in density. Consequently, composites from MFESA were selected for thermal conductivity testing at elevated temperatures, and the results are presented in Fig. 13(b). The thermal conductivity values obtained are 0.058 W/(m·K) at 600 °C, 0.075 W/(m·K) at 800 °C, and only 0.108 W/(m·K) at 1000 °C.

3.6.2 Thermal insulation properties

To provide further confirmation of the thermal insulation capability of the samples, a butane torch was used to ablate the annealed samples of different fiber-reinforced materials on one side (with a flame temperature of 1300 °C). During a duration of 600 s, the temperature change on the rear surface of the samples was recorded via thermocouples, while an infrared camera was used to monitor the temperature distribution on the same surface. The results obtained are shown in Fig. 14 (from left to right, the samples after annealing for 2 h at 1100, 1200, and 1300 °C). A detailed analysis of samples from four different reinforcing fiber materials revealed that their thermal insulation performance significantly decreased as the annealing temperature increased. However, the temperature difference between the heated and cooled surfaces remained above 1070 °C, which ensured that optimal thermal insulation capabilities were maintained. The cold surface temperature of DFESA (Fig. 14(d)), which was annealed at 1300 °C for 2 h, reached 150 °C after 150 s and subsequently stabilized. A comparative analysis revealed that both MFESA-1050 and DFESA-1050 exhibited optimal thermal insulation performance, with the lowest recorded back temperature of approximately 110 °C.

4 Discussion

4.1 Synthesis and confirmation of $(YYbErDyGd)_2SiO_5$ ceramic aerogels

The ESA-1050 sample obtained is shown in Fig. 15(a) and is stable enough to be maintained on the stamen. XRD analysis (Fig. 1(b)) combined with TG–DSC (Fig. 3(b)) revealed endothermic peaks, indicating that the high-entropy formation temperature was in the range of 950–1050 °C and approximately 1040 °C. Furthermore, in Fig. 1(b), the presence of $[SiO_4]$, $[REO_7]$, and $[REO_9]$ groups in

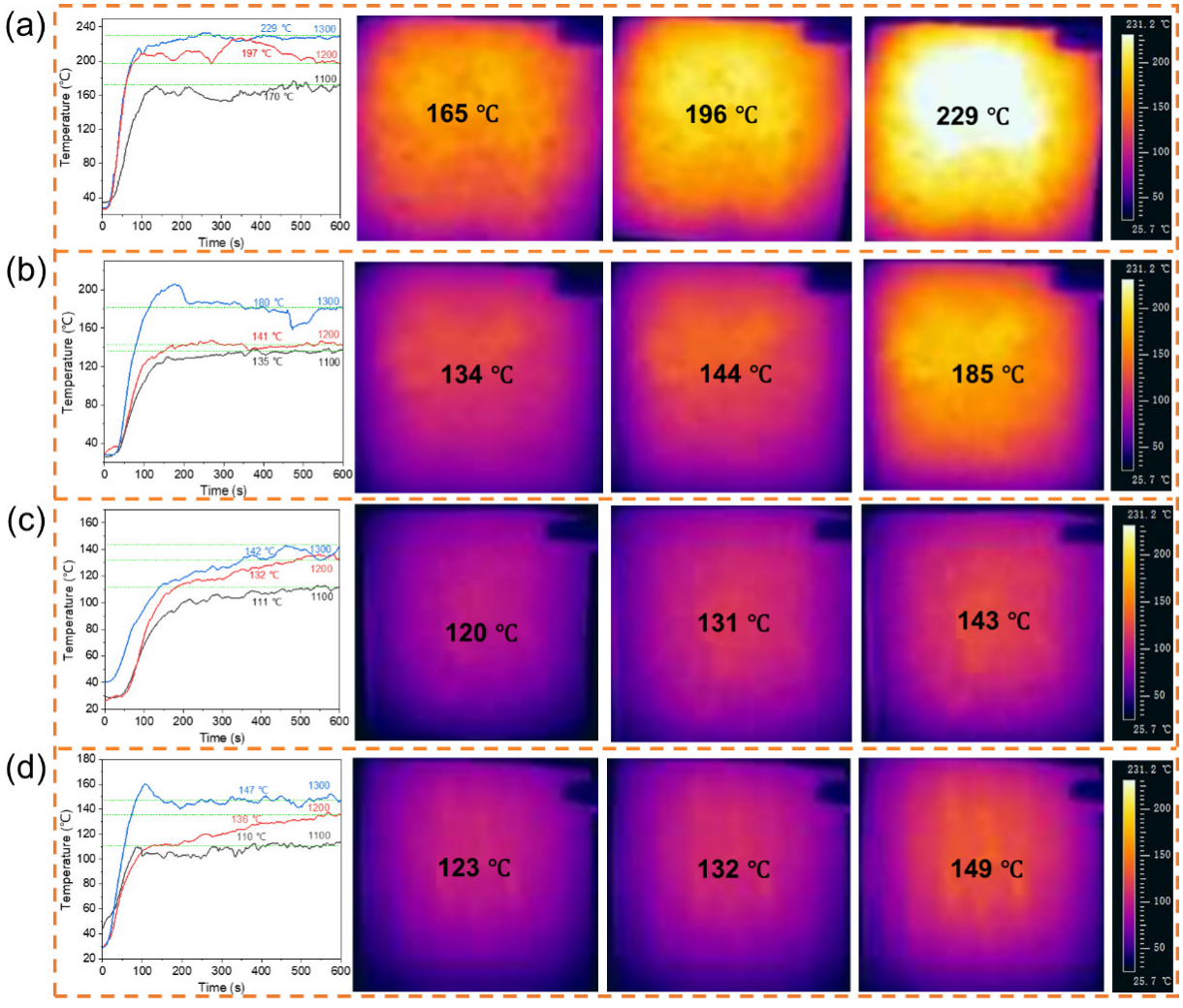

Fig. 14 Infrared images and temperature evolution on back side of different fiber-reinforced high-entropy aerogels exposed to a butane torch flame at 1300 °C for 600 s: (a) XFESA-1050; (b) GFESA-1050; (c) MFESA-1050; (d) DFESA-1050.

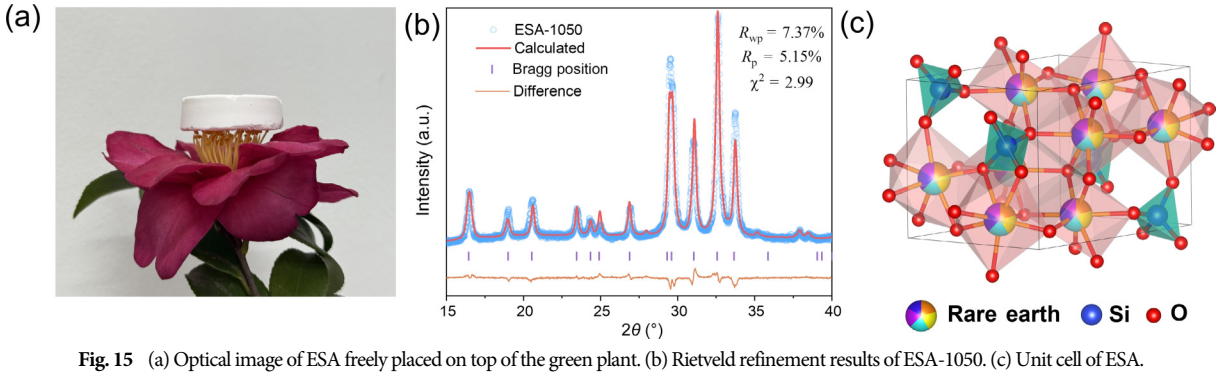

Fig. 15 (a) Optical image of ESA freely placed on top of the green plant. (b) Rietveld refinement results of ESA-1050. (c) Unit cell of ESA.

the Raman results indicates the formation of X1-RE_2SiO_5. The appearance of these peaks in the FTIR spectrum in Fig. 3(a) confirms the formation of the monosilicate structure, indicating successful structural development during the calcination process. When the temperature was increased to 1350 °C, a partial crystalline transition may have occurred because of the excessively high temperature. The peaks that appeared at approximately 911 cm^{-1} are speculated to belong to REO_6 ligands in the compound X2-RE_2SiO_5. However, owing to their limited quantity, the characteristic peaks of X2-RE_2SiO_5 were not detected in the XRD analysis. Overall, the results of the FTIR spectroscopy are consistent with the findings from the XRD and Raman analyses. This observation is indicative of the successful synthesis of ESAs.

The objective is to verify the crystal structure of the obtained ESA sample. The Rietveld refinement XRD results (Fig. 15(b)) were obtained via general structural analysis system (GSAS) software, yielding low fit factors of R_{wp} = 7.37% and X^2 = 2.99. The refined cell parameters (a = 6.67 Å, b = 6.9 Å, and c = 9.02 Å) were found to be in good agreement with their mean values, indicating the reliability of the results. The ideal crystal structure of X1-RE_2SiO_5 is shown in Fig. 15(c). Consequently, the synthesized ESA is classified within the monoclinic crystal system, which

aligns with the characteristics of X1-RE_2SiO_5 and has a space group of $P2_1/c$. The ball-and-stick model provides a clear visual representation of the atomic occupation in the five-cation ESA material. In this model, the red ball represents the oxygen atom, which is arranged in a silicon-centered tetrahedron with a green silicon atom. The colored balls indicate that the cationic sites are randomly occupied by five metal cations, each with an equal probability of occupancy. The configurational entropy of the oxide (S_{config}) is calculated to be 1.61R according to Eq. (7):

$$S_{config} = -R\left(\left(\sum_{i=1}^{N} x_i \ln x_i\right)_{cation\text{-}site} + \left(\sum_{j=1}^{N} x_j \ln x_j\right)_{anion\text{-}site}\right) \quad (7)$$

where x_i and x_j denote the molar ratios at the cation and anion sites, respectively. R is the universal gas constant.

The compositional distribution of ESAs, as displayed in Fig. 2(g), confirms that several elements (Y, Yb, Er, Dy, and Gd) are distributed homogeneously, showing no signs of segregation or the presence of a second phase. Therefore, the consistent characterization results obtained from XRD, XPS, Raman spectroscopy, and EDS collectively support the successful synthesis of ESAs. These analyses indicate that the synthesized high-entropy silicate ceramic aerogel samples are chemically and structurally homogeneous solid solutions, lacking surface segregation or phase separation, featuring a single-phase X1-RE_2SiO_5 structure [42,43].

The formation of high-entropy silicates has been proven through phase composition analysis. In addition, the microstructure and pore structure of high-entropy ceramic aerogels have been explored primarily through SEM and BET analysis. The SEM image indicates that the sample at 1350 °C did not undergo sintering (Fig. 5(e)), allowing the ceramic aerogel to retain its porous nature, which is advantageous for its thermal insulation properties at high temperatures. However, the grains demonstrate a substantial increase in size and an increase in the diameter of the pores. The BET results (Figs. 5(p)–5(t)) also indicate a reduced proportion of small pores alongside an increased proportion of larger pores, which aligns well with the SEM analysis. This decrease can be attributed to the decomposition of organic matter during heat treatment, which results in the formation of macropores within the aerogel structure. The consistency between the BJH analysis and SEM observations further supports the characterization of the pore structure in the ESA-SCD samples. The high specific surface area of ESA-SCD supports the effective completion of solid-phase sintering during heat treatment. Furthermore, the XRD pattern (Fig. 1(b)) shows that an increase in the calcination temperature from 950 to 1350 °C resulted in a sharpening of the characteristic peaks of the high-entropy ceramic aerogels. This finding suggests that the crystallinity of the X1-RE_2SiO_5 crystal structure improves, whereas the peak positions remain constant, indicating that the grains grow in accordance with the temperature. On the basis of the above analysis, a $(YYbErDyGd)_2SiO_5$ ceramic aerogel was successfully synthesized.

4.2 Analysis of high-temperature stability of ESA

As a high-temperature insulation material, the high-temperature stability of the material itself is of paramount importance. Consequently, the high-entropy ceramic aerogel that was synthesized was subjected to annealing at temperatures ranging from 1200 to 1600 °C for 2 h in an air atmosphere (Fig. 6). At temperatures in excess of 1300 °C, a phase transition is observed. Owing to prolonged exposure to high temperatures, the crystalline phase of high-entropy monosilicate undergoes a phase transformation from X1-RE_2SiO_5, which is synthesized at low temperatures, to the more stable X2-RE_2SiO_5 phase at high temperatures, thereby achieving the goal of withstanding higher temperatures. Furthermore, the Rietveld refinement results were obtained via GSAS-II software (Fig. 16(a)). A comparison of the calculated diffraction patterns with the experimentally obtained XRD patterns reveals a minimal error. This indicates the reliability of the diffraction patterns generated through the calculation and refinement process (low fitting factors: R_{wp} = 6.65%, R_p = 4.47%, X^2 = 1.39). The crystal structure model of X2-RE_2SiO_5 was obtained via VESTA. It incorporates [SiO_4], [REO_6], and [REO_7] coordination polyhedra and belongs to the monoclinic crystal system with the space group C_2/c, as shown in Fig. 16(b). In conclusion, the $(YYbErDyGd)_2SiO_5$ high-entropy ceramic aerogel

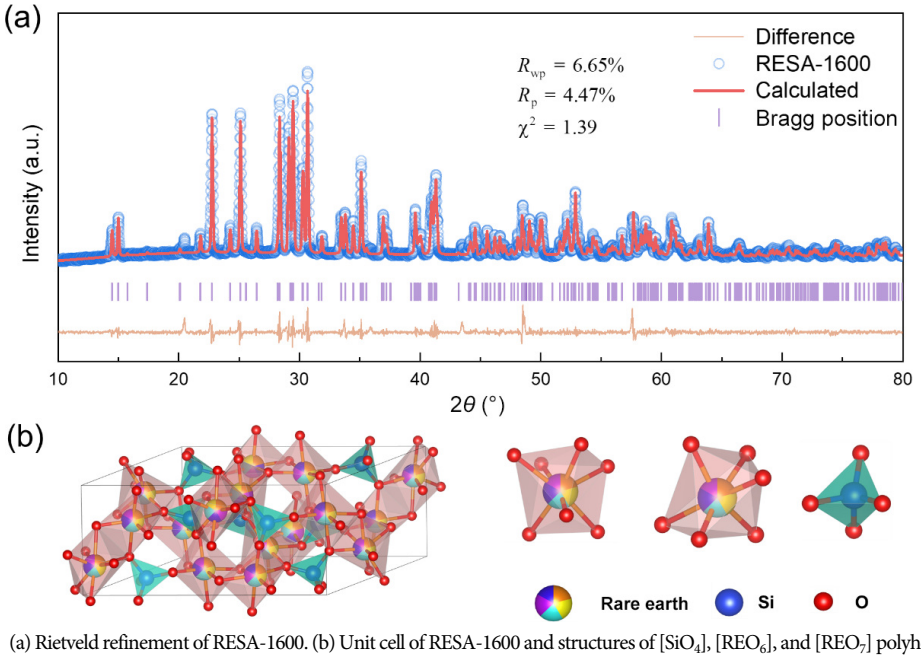

Fig. 16 (a) Rietveld refinement of RESA-1600. (b) Unit cell of RESA-1600 and structures of [SiO_4], [REO_6], and [REO_7] polyhedrons.

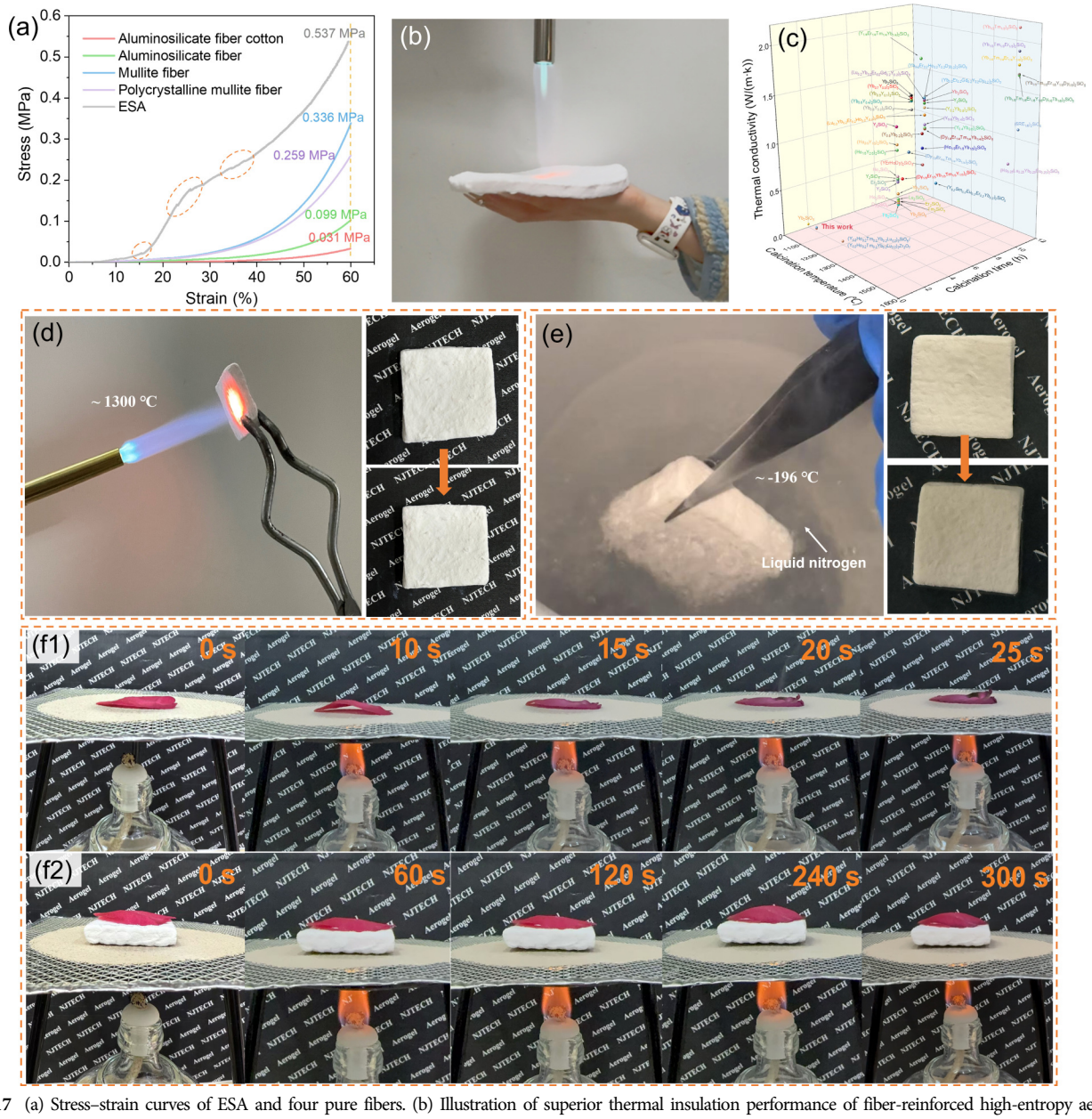

Fig. 17 (a) Stress–strain curves of ESA and four pure fibers. (b) Illustration of superior thermal insulation performance of fiber-reinforced high-entropy aerogel. (c) Summary of recently reported representative data for monosilicates. (d) Optical image of fiber-reinforced high-entropy aerogel exposed to a butane torch flame (~1300 °C). (e) Immersion in liquid nitrogen for 5 min (approximately−196 °C). (f) Photographs of flower petals positioned on aerogel textiles that remained fresh under a high-temperature alcohol lamp (f2) for 300 s, whereas petals lacking aerogel insulation exhibited evident signs of withering and carbonization (f1) after 25 s.

was stabilized to the X2-RE_2SiO_5 phase during a 2-h assessment period at temperatures between 1300 and 1600 °C. This process occurred without creating any additional impurities, demonstrating exceptional high-temperature phase stability.

In addition, Fig. 7 shows the changes in the grain size and pore size in the temperature range of 1200–1600 °C. As illustrated in Figs. 7(a)–7(o), the grain size of the RESA gradually increased with increasing annealing temperature. This phenomenon can be attributed to the fact that elevated temperatures provide the energy required for atoms or molecules to migrate. Consequently, processes such as volume diffusion and grain boundary diffusion are initiated, leading to a substantial increase in the rate of material transport. This results in accelerated thickening of the necks, thereby coarsening the backbone. Moreover, the ceramic spheres illustrated in Figs. 7(g) and 7(h) may be composed of $RE_2Si_2O_7$. RE_2SiO_5 reacts with SiO_2 at elevated temperatures, resulting in the formation of $RE_2Si_2O_7$ [44]. In addition, aerogels tend to undergo shrinkage and structural rearrangement at elevated temperatures, resulting in the formation of local compositional inhomogeneities. Under such conditions, the silicate phases may undergo local melting and subsequent recrystallization. The formation of silicate liquid or semiliquid phases is transient, and these locally molten regions can shrink into spherical shapes under the influence of surface tension. Upon cooling and solidification, smooth-surfaced ceramic spheres are formed. High-magnification EDS images of the RESA-1300 sample were obtained (Fig. 8). The results demonstrated that the ceramic sphere regions exhibited a significantly strong Si signal, indicating substantial Si enrichment. This finding is consistent with the higher Si content observed in $RE_2Si_2O_7$ than that in RE_2SiO_5. However, no diffraction peaks corresponding to $RE_2Si_2O_7$ were observed in the XRD pattern (Fig. 6), which may be attributed to its limited formation amount or high dispersion, resulting in concentrations below the detection threshold. The

results of the morphological and compositional analyses indicate that the ceramic spheres are predominantly composed of locally formed $RE_2Si_2O_7$ phases.

Furthermore, the specific surface area decreases with increasing temperature (Figs. 7(p)–7(t)). This can be attributed to the high temperatures causing the pore walls of the aerogel skeleton to thicken, which leads to the merging of some small pores into larger macropores [45]. This finding was subsequently corroborated by XRD analysis (Fig. 6). The local magnification of the XRD patterns clearly shows that the diffraction peaks shifted slightly to the left with increasing annealing temperature. This shift is attributed to peak movement resulting from grain growth at high temperatures, which is accompanied by an increase in the volume of the grain cells [46]. Consequently, the ESA itself not only exhibits good phase stability but also maintains a porous structure at 1600 °C, thereby demonstrating excellent high-temperature thermal stability.

4.3 Analysis of compressive strength and thermal insulation properties of fiber-reinforced high-entropy aerogels

The compressive strength of the ESA was enhanced through the incorporation of fiber materials. Figure 17(a) shows the stress–strain curves of the ESA and four pure fiber materials. The ESA results in better compressive strength, reaching a maximum of 0.537 MPa at 60% strain. However, the curve lacks smoothness, as evidenced by the steps highlighted in the orange circles, which indicate varying degrees of cracking in the ESA. A comparison of the compressive strength curves (Fig. 12) of the pure fibers with those of the fiber-reinforced materials reveals a significant enhancement in the mechanical properties of the latter. This enhancement occurs because some of the fibers gradually melt at higher temperatures, leading to the agglomeration of the fibers and a reduction in material volume, which is the primary reason for the significant increase in density shown in Fig. 11(a). Moreover, as the annealing temperature increases, the fiber reinforcement undergoes partial sintering and fracture, while some pore channels collapse or coalesce. This results in a reduction in pore volume and thickening of the pore walls. Consequently, both the specific surface area and porosity decrease (Fig. 11(b) and Table 4). However, the mechanical properties of MFESA and DFESA generally decrease, which can be attributed to the physical aging of the fiber mat matrix at elevated temperatures. This leads to structural damage and subsequent spalling from the aerogel, thus reducing its ability to effectively withstand transfer loads. In comparison, mullite demonstrates a higher degree of resistance to high temperatures than does aluminosilicate. This is evidenced by the absence of a significant change in density in Fig. 11(a). Therefore, although the compressive strengths of MFESA and DFESA exhibited a downward trend, the lowest recorded values were still 0.193 and 0.026 MPa (60% strain), respectively. Furthermore, the shrinkage rate was minimal, and the high-temperature stability was superior (the porosity of MFESA-1300 was 83.11%), indicating that MFESA and DFESA have more promising application prospects at elevated temperatures.

In high-entropy materials, the presence of oxygen vacancies (Fig. 2(f)) can significantly influence their properties. These vacancies can lead to lattice distortions and irregularities, which may serve as nucleation sites for dislocations. For example, the dislocations are indicated in the HRTEM image in Fig. 4(b). This phenomenon can affect the hardness and strength of the material, as the dislocations can alter how the material deforms under stress. Additionally, the presence of oxygen vacancies can disrupt atomic vibrations, which in turn affects the thermodynamic transport properties of the material. This disruption may result in variations in the thermal conductivity throughout the lattice. An increase in potential oxygen vacancies could improve the thermal and mechanical properties of ESAs [47]. As shown in Fig. 13, MFESA demonstrates optimal thermal stability, exhibiting a marginal increase in thermal conductivity of only 0.004 W/(m·K) from 1100–1300 °C, with minimal change. Compared with pure fiber materials, MFESA and DFESA clearly exhibit reduced thermal conductivity (Table 5). Figure 17(c) shows a comparison of the synthesis temperature, calcination time, and thermal conductivity of the fiber-reinforced materials obtained in this work with those of related rare-earth metal materials. It is clear that the prepared fiber-reinforced materials demonstrate low thermal conductivity. This property makes them particularly beneficial for high-temperature thermal insulation applications. As depicted in Fig. 17(b), the fiber-reinforced sample, with a thickness of 12 mm, effectively prevents hand burns even after being heated with a butane torch for over 0.5 min.

Figure 17(d) presents the front side of the sample that was ablated via a butane torch to simulate a high-temperature, harsh environment. The dimensions of the sample are specified as 30 mm × 30 mm × 10 mm. Figure 17(e) depicts the same sample after it was placed in liquid nitrogen for 5 min. The sample clearly exhibited no discernible damage or deformation prior to or subsequent to this process. They can endure butane torch flame temperatures up to 1300 °C and liquid nitrogen temperatures as low as −196 °C. This broad operating temperature range highlights their significant potential for applications in extreme environments [48]. In addition, freshly picked petals were placed on an asbestos screen and heated with an alcohol lamp. The flowers exhibited significant charring under sustained burning for 25 s (Fig. 17(f1)). In contrast, another petal was well protected by a fiber-reinforced high-entropy ceramic aerogel sample with a thickness of 10 mm, which remained intact even after 300 s of heating, with only minor burns on the edges (Fig. 17(f2)). In summary, combining Figs. 13 and 14, the prepared fiber-reinforced high-entropy ceramic aerogels exhibit low thermal conductivity, exceptional thermal insulation and ablation resistance, and a decrease in the likelihood of spontaneous combustion, which holds considerable practical application value.

The objective of this study is to assess the effects of thermal cycling on the structure and mechanical properties of samples. The samples from the MFESA were subjected to a series of thermal cycling tests in air at a temperature of 1300 °C for 2 h per cycle, with a total of 20 cycles performed. Microstructural and thermomechanical analyses were conducted after the 1st, 5th, 15th, and 20th cycles, respectively (Figs. 18 and 19). The corresponding samples are denoted as MFESA-1300, MFESA-1300/5C, MFESA-1300/15C, and MFESA-1300/20C.

The XRD pattern of the MFESA-1300 sample is presented in Fig. 18(a). A comparison with standard PDF cards indicates that the diffraction peaks correspond to the X2-RE_2SiO_5 and mullite phases, suggesting that the MFESA sample has good phase stability at elevated temperatures. However, after 20 thermal cycles (Fig. 18(b)), diffraction peaks associated with the $RE_2Si_2O_7$ phase appeared in the MFESA-1300/20C sample. This transformation is likely attributed to the reaction between SiO_2 enriched within the fiber matrix and RE_2SiO_5 during repeated high-temperature cycling, leading to the formation of $RE_2Si_2O_7$ (Reaction (8)). The conversion process is facilitated by high temperatures and enhanced grain diffusion during cycling. The increased Si

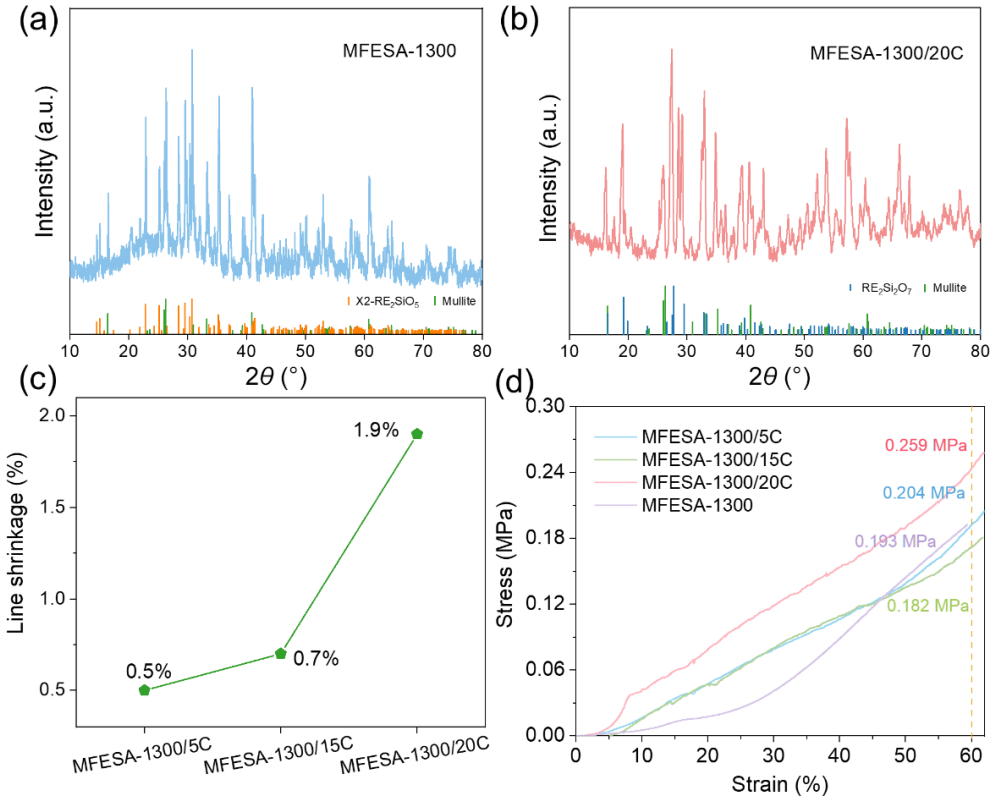

Fig. 18 (a, b) XRD pattern, (c) line shrinkage, and (d) strain–stress curves of MFESA-1300 and its thermal cycling samples.

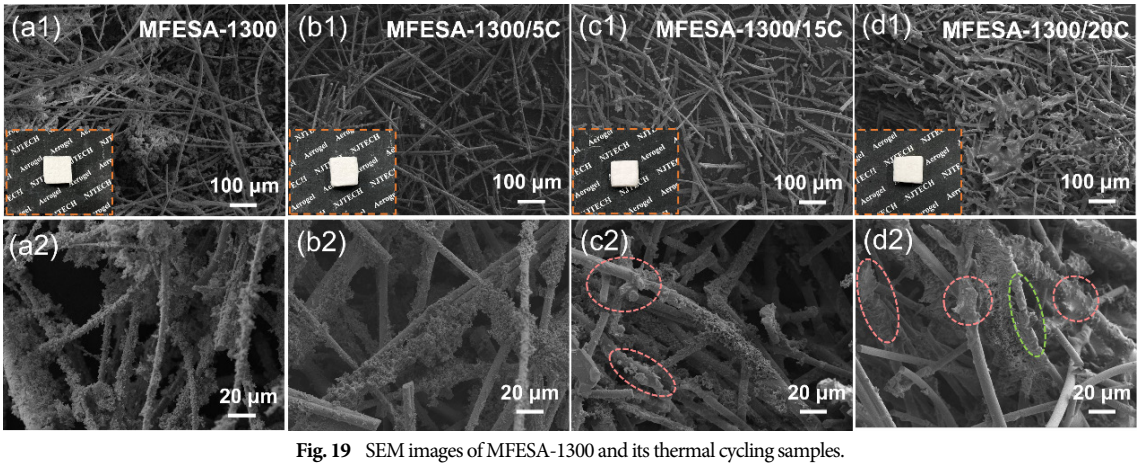

Fig. 19 SEM images of MFESA-1300 and its thermal cycling samples.

diffusion and local enrichment at elevated temperatures further promote the thermodynamic driving force for $RE_2Si_2O_7$ formation, thereby inducing the observed phase transition (Reaction (8)):

$$RE_2SiO_5 + SiO_2 \rightarrow RE_2Si_2O_7 \quad (8)$$

Moreover, as shown in Fig. 18(c), the linear shrinkage of the sample exhibited negligible variation after 15 thermal cycles, remaining as low as 0.7%, and only increased to 1.9% after 20 cycles. This indicates that slight sintering shrinkage occurred after multiple cycles, while the overall structure retained excellent dimensional stability. The stress–strain curves (Fig. 18(d)) show that the profiles gradually become rougher with an increasing number of cycles, suggesting the formation of localized microcracks and structural rearrangement during compression. This phenomenon was particularly evident in the MFESA-1300/15C and MFESA-1300/20C samples. At a deformation of 60%, the compressive strength of MFESA-1300/20C exhibited a noticeable enhancement, which may be attributed to partial sintering and densification of the fiber matrix at elevated temperatures. The resulting increase in apparent density led to increased compressive strength under identical deformation conditions.

To further elucidate the effect of thermal cycling on microstructural evolution, SEM was performed on samples subjected to different numbers of thermal cycles (Fig. 19). After 5 cycles, MFESA-1300/5C exhibited partial fiber fracture (Fig. 19(b1)), whereas no apparent signs of sintering were detected (Fig. 19(b2)). After 15 cycles, evident sintering was observed in localized regions (highlighted by red circles in Fig. 19(c2)). After 20 cycles, distinct melting (green circle in Fig. 19(d2)) and agglomeration (red circles in Fig. 19(d2)) phenomena appeared between adjacent fibers. This progressive microstructural evolution is consistent with the formation of the $RE_2Si_2O_7$ phase identified by XRD, as well as the

Table 6 Density and thermal conductivity of MFESA-1300 and its thermal cycling samples

Sample	Density (g/cm³)	Thermal conductivity (W/(m·K))
MFESA-1300	0.245	0.034
MFESA-1300/5C	0.287	0.035
MFESA-1300/15C	0.298	0.038
MFESA-1300/20C	0.311	0.043

concomitant enhancement in compressive strength. However, since the macroscopic morphology, linear shrinkage, and density of the samples did not significantly vary, the room-temperature thermal conductivity of the MFESA-1300/20C sample remained relatively low, reaching only 0.043 W/(m·K) (Table 6). In summary, the prepared fiber-reinforced high-entropy ceramic aerogel exhibits low thermal conductivity, excellent thermal insulation, and ablation resistance while reducing the risk of spontaneous combustion. Moreover, the MFESA sample demonstrates outstanding phase stability and structural integrity under high-temperature thermal cycling, maintaining low thermal conductivity and satisfactory mechanical properties even after 20 cycles, thereby showing exceptional thermal cycling resilience. These characteristics highlight the material's considerable potential and practical value as an advanced thermal insulation solution for extremely high-temperature environments.

5 Conclusions

In summary, we successfully prepared $(YYbErDyGd)_2SiO_5$ high-entropy ceramic aerogels via the sol–gel method with formamide as a templating agent. In addition, different fiber-reinforced ceramic aerogel composites have also been explored. The key conclusions are as follows:

(1) The $(YYbErDyGd)_2SiO_5$ high-entropy ceramic aerogels were prepared at 1050 °C, and they were stabilized to the X2-RE_2SiO_5 phase after being annealed at 1300–1600 °C for 2 h. Meanwhile, there were no sintering or melting phenomena at 1600 °C for 2 h, resulting in excellent high-temperature thermal stability.

(2) A comparison of different fiber-reinforced materials revealed that the MFESA-1050 material had low thermal conductivities of 0.032 W/(m·K) at 25 °C and 0.108 W/(m·K) at 1000 °C. Furthermore, the compression strength reached 0.327 MPa (60% compression deformation) following a 2-h examination at 1200 °C. They demonstrate no visible damage or deformation under extreme conditions across a substantial temperature range, ranging from −196 to 1300 °C.

(3) The temperature difference between the hot and cold surfaces of the fiber-reinforced materials was as high as 1200 °C after 600 s of ablation at 1300 °C, butane torch, which exhibited excellent ablation resistance and thermal insulation properties. Moreover, even after 20 high-temperature thermal cycles (1300 °C, 2 h), the MFESA sample maintained a low thermal conductivity of 0.043 W/(m·K) and a satisfactory compressive strength of 0.259 MPa.

(4) Consequently, it possesses considerable potential as an ultrahigh-temperature thermal protection material for utilization as a heat-sealing end material and heat-insulating material for components subjected to elevated temperatures in aerospace vehicles, ships, and other equipment.

Acknowledgements

This work was financially supported by the National Natural Science Foundation of China (No. 52272300), the Jiangsu Collaborative Innovation Center for Advanced Inorganic Function Composites, and the Priority Academic Program Development of Jiangsu Higher Education Institutions.

Availability of data and materials

The data that support the findings of this study are available from the corresponding author upon reasonable request.

Competing interests

The authors have no competing interests to declare that are relevant to the content of this article.

References

[1] Liu Y, Su HJ, Shen ZL, *et al.* Effect of seed orientations on crystallographic texture control in faceted Al_2O_3/YAG eutectic ceramic during directional solidification. *J Mater Sci Technol* 2023, **146**: 86–101.

[2] Duan BH, Mao L, Lv MR, *et al.* Interface interaction during the preparation of TiAl–(Nb,V) quaternary intermetallic single crystals by directional solidification based on Y_2O_3 doped $BaZrO_3/Al_2O_3$ composite ceramic mold. *J Eur Ceram Soc* 2023, **43**: 5032–5043.

[3] Chen ZY, Wang YZ, Huang YL, *et al.* Medium-entropy monosilicates deliver high corrosion resistance to calcium–magnesium aluminosilicate molten salt. *Adv Sci* 2024, **11**: 2400736.

[4] Almishal SSI, Furst M, Tan YZ, *et al.* Thermodynamics-inspired high-entropy oxide synthesis. *Nat Commun* 2025, **16**: 8211.

[5] Oses C, Toher C, Curtarolo S. High-entropy ceramics. *Nat Rev Mater* 2020, **5**: 295–309.

[6] Chen ZL, Tian ZL, Zheng LY, *et al.* $(Ho_{0.25}Lu_{0.25}Yb_{0.25}Eu_{0.25})_2SiO_5$ high-entropy ceramic with low thermal conductivity, tunable thermal expansion coefficient, and excellent resistance to CMAS corrosion. *J Adv Ceram* 2022, **11**: 1279–1293.

[7] Liu T, Ma BY, Zan WY, *et al.* Green preparation of high entropy ceramics $(Y_{0.2}Sm_{0.2}Eu_{0.2}Er_{0.2}Yb_{0.2})_2SiO_5$ with low thermal conductivity by molten salt synthesis. *Ceram Int* 2024, **50**: 2718–2726.

[8] Wei P, Zhao SX, Zhuang L, *et al.* Chemical co-precipitation synthesis of high-entropy rare-earth silicate nanopowders. *J Am Ceram Soc* 2024, **107**: 3577–3586.

[9] Xu X, Zhang QQ, Hao ML, *et al.* Double-negative-index ceramic aerogels for thermal superinsulation. *Science* 2019, **363**: 723–727.

[10] Xiao W, Lu LJ, Xu ZJ, *et al.* A superelastic ceramic aerogel for flexible pressure sensor in harsh environment. *Compos Part B—Eng* 2025, **292**: 112110.

[11] Luo JW, Lv Z, Zhang LP, *et al.* Modulation of dielectric behavior in ceramic-based materials for integrated electromagnetic waves absorption and thermal conduction. *Adv Funct Mater* 2025, **35**: 2420086.

[12] Liu XN, Su CX, Zhong Y, *et al.* High entropy $(LaCeSmEuNd)_2Zr_2O_7$ ceramic aerogel with low thermal conductivity and excellent structural heat resistance. *J Eur Ceram Soc* 2022, **42**: 5964–5972.

[13] Wang DL, Song CY, Dang SX, *et al.* High-entropy ceramic aerogel with ultrahigh thermomechanical properties. *ACS Appl Mater Inter* 2025, **17**: 18636–18644.

[14] Han YQ, Wu YQ, Huang S, *et al.* High-temperature thermal stability modification of $(La_{0.2}Y_{0.2}Sm_{0.2}Eu_{0.2}Nd_{0.2})_2Zr_2O_7$ ceramic aerogel for enhanced thermal insulation performance. *Ceram Int* 2024, **50**: 22010–22017.

[15] Si Y, Yu JY, Tang XM, *et al.* Ultralight nanofibre-assembled cellular aerogels with superelasticity and multifunctionality. *Nat Commun* 2014, **5**: 5802.

[16] Mei H, Li H, Jin ZP, *et al.* 3D-printed SiC lattices integrated with lightweight quartz fiber/silica aerogel sandwich structure for thermal protection system. *Chem Eng J* 2023, **454**: 140408.

[17] Wang HL, Lin S, Yang S, *et al.* High-temperature particulate matter

filtration with resilient yttria-stabilized ZrO_2 nanofiber sponge. *Small* 2018, **14**: 1800258.

[18] Dang SX, Guo JR, Deng YP, *et al.* Highly-buckled nanofibrous ceramic aerogels with ultra-large stretchability and tensile-insensitive thermal insulation. *Adv Mater* 2025, **37**: 2415159.

[19] Jiang JP, Yan LW, Li JT, *et al.* Lightweight, thermally insulating SiBCN/Al_2O_3 ceramic aerogel with enhanced high-temperature resistance and electromagnetic wave absorption performance. *Chem Eng J* 2024, **501**: 157656.

[20] Wang XZ, Li HM, Li HY, *et al.* Coaxial porous SiBCN/SiCN ceramic fiber aerogels with reduced shrinkage and low thermal conductivity. *Chem Eng J* 2024, **501**: 157621.

[21] Zhang X, Yu JY, Si Y. Programmable shape-morphing enables ceramic meta-aerogel highly stretchable for thermal protection. *Adv Mater* 2025, **37**: 2412962.

[22] Zheng LH, Zhao GJ, Yan CF, *et al.* Raman spectroscopic investigation of pure and ytterbium-doped rare earth silicate crystals. *J Raman Spectrosc* 2007, **38**: 1421–1428.

[23] Haumesser PH, Gaumé R, Viana B, *et al.* Spectroscopic and crystal-field analysis of new Yb-doped laser materials. *J Phys—Condens Mat* 2001, **13**: 5427–5447.

[24] Sakar N, Akalin SA, Yavas A, *et al.* Ce and Gd doped ZnO nanorods: A study on structural, optical, and photocatalytic enhancements. *J Alloy Compd* 2025, **1021**: 179672.

[25] Wang YW, Niu YR, Zhong X, *et al.* Water vapor corrosion behaviors of plasma sprayed RE_2SiO_5 (RE = Gd, Y, Er) coatings. *Corros Sci* 2020, **167**: 108529.

[26] Xia YJ, Chen GB, Zhang Z, *et al.* Nanowire-filled layered SiC aerogels with excellent thermodynamic properties for thermal insulation at ultrahigh temperatures. *Chem Eng J* 2025, **510**: 161479.

[27] Qin M, Zhang LM, Zhao XR, *et al.* Defect induced polarization loss in multi-shelled spinel hollow spheres for electromagnetic wave absorption application. *Adv Sci* 2021, **8**: 2004640.

[28] Zhao SX, Wei P, Zhuang L, *et al.* Rapid combustion synthesis of high-entropy rare-earth silicate nanopowders via SiO_2 templates. *Ceram Int* 2024, **50**: 31006–31013.

[29] Liu XN, Wang J, Su CX, et.al. Porous medium-entropy $(Zr_{0.25}Ce_{0.25}Hf_{0.25}Y_{0.25})O_{2-\delta}$ ceramic with low thermal conductivity: using aerogel structure as the precursor. *Ceram Int* 2023, **49**: 36071–36079.

[30] Shang SS, Wang J, Yuan M, *et al.* Characterization and thermal properties of $(YErYbGdLa)_2Zr_2O_7$ high entropy ceramic aerogel. *Mater Charact* 2024, **217**: 114392.

[31] Kissikov T, Sarkar R, Lawson M, *et al.* Uniaxial strain control of spin-polarization in multicomponent nematic order of $BaFe_2As_2$. *Nat Commun* 2018, **9**: 1058.

[32] Lu MX, Fang Y, Xu XY, *et al.* Non-equimolar bismuth-layered $[Ca_xSr_{(1-x)/3}Ba_{(1-x)/3}Pb_{(1-x)/3}]Bi_4Ti_4O_{15}$ high-entropy ceramics with high curie temperature. *J Materiomics* 2025, **11**: 100945.

[33] Su L, Ren JK, Lu T, *et al.* Deciphering structural origins of highly reversible lithium storage in high entropy oxides with *in situ* transmission electron microscopy. *Adv Mater* 2023, **35**: 2205751.

[34] Yang XM, An ZB, Zhai YD, *et al.* Effect of Al content on the thermal oxidation behaviour of AlHfMoNbTi high-entropy alloys analysed by *in situ* environmental TEM. *Corros Sci* 2021, **191**: 109711.

[35] Yu HJ, Tong ZW, Yue S, *et al.* Effect of SiO_2 deposition on thermal stability of Al_2O_3–SiO_2 aerogel. *J Eur Ceram Soc* 2021, **41**: 580–589.

[36] Yan NN, Shi XH, Li K, *et al.* Adsorption properties and preparation of porous TaC ceramics with regular steps. *J Alloy Compd* 2018, **731**: 971–977.

[37] Sing KSW. Adsorption methods for the characterization of porous materials. *Adv Colloid Interfac* 1998, **76–77**: 3–11.

[38] Shang SS, Wang J, Wang ZH, *et al.* A novel Yb_2SiO_5 ceramic aerogel with excellent thermal stability for high-temperature thermal insulation. *Ceram Int* 2024, **50**: 50133–50144.

[39] Pan YL, He S, Gong LL, *et al.* Low thermal-conductivity and high thermal stable silica aerogel based on MTMS/water-glass co-precursor prepared by freeze drying. *Mater Design* 2017, **113**: 246–253.

[40] Fan D, Zhong X, Zhang ZZ, *et al.* Investigation on behavior and mechanism of enhanced water vapor corrosion resistance for $(Lu_{0.25}Yb_{0.25}Er_{0.25}Y_{0.25})_2SiO_5$ environmental barrier coating. *J Eur Ceram Soc* 2023, **43**: 3737–3745.

[41] Tian ZL, Ming KY, Zheng LY, *et al. In-situ* observation and mechanism of calcium–magnesium–alumina–silicate (CMAS) melts-induced degradation of RE_2SiO_5 (RE = Tb, Dy, Ho, Y, Er, Tm, and Yb) ceramics at 1500 °C. *J Adv Ceram* 2023, **12**: 2315–2330.

[42] Sun Z, Zhao YJ, Sun C, *et al.* High entropy spinel-structure oxide for electrochemical application. *Chem Eng J* 2022, **431**: 133448.

[43] Fan D, Zhong X, Zhang ZZ, *et al.* Interaction of high-entropy rare-earth monosilicate environmental barrier coatings subjected to corrosion by calcium–magnesium–alumino–silicate melts. *Corros Sci* 2022, **207**: 110564.

[44] He YX, Wang X, Wang C, *et al.* Significantly improved corrosion resistance of high-entropy rare-earth silicate multiphase ceramics against molten CMAS. *J Am Ceram Soc* 2023, **106**: 2744–2751.

[45] Hao W, Lu XZ, Li L, *et al.* Toughened $(Ti_{0.2}Zr_{0.2}Hf_{0.2}Nb_{0.2}Ta_{0.2})B_2$–SiC composites fabricated by one-step reactive sintering with a unique SiB_6 additive. *J Adv Ceram* 2024, **13**: 86–100.

[46] Liew SL, Zhou J, Wei FX, *et al.* Design and synthesis of single phase $Hf_{0.25}Zr_{0.25}Ce_{0.25}Y_{0.125}Si_{0.125}O_{2-\delta}$ high-entropy ceramics. *J Alloy Compd* 2022, **904**: 164097.

[47] Hou JD, Liu YF, Cheng CF, *et al.* Thermal properties of high-entropy fluorite $(Zr_{0.2}Hf_{0.2}Pr_{0.2}La_{0.2}X_{0.2})O_{2-\delta}$ (X = Dy, Ho, Er, Y, Tm): A first-principles combined with experimental study investigating the influence of size and mass difference effect. *J Alloy Compd* 2024, **996**: 174774.

[48] You Q, Wu ZY, Li YJ, *et al.* Amorphous SiOC-coated submicron mullite aerogels with excellent thermal and structural stability up to 1500 °C. *J Eur Ceram Soc* 2025, **45**: 117079.